Transient torque reversals in indirect drive wind turbines

Saptarshi Sarkar[1,2], Håkan Johansson[3], Viktor Berbyuk[3], and Present Address[3]

[1]Saptarshi Sarkar, Department of Mechanics and Maritime Sciences, Department of Mechanics and Maritime Sciences, Chalmers University of Technology
[2]Chalmers University of Technology
[3]Affiliation not available

March 17, 2023

Transient torque reversals in indirect drive wind turbines

Saptarshi Sarkar* | Håkan Johansson | Viktor Berbyuk

[1]Department of Mechanics and Maritime
Sciences, Chalmers University of
Technology, Gothenburg, Sweden

Correspondence
*Saptarshi Sarkar, Department of Mechanics
and Maritime Sciences, Chalmers University
of Technology, Gothenburg, Sweden. Email:
ssarkar@chalmers.se

Present Address
Department of Mechanics and Maritime
Sciences, Chalmers University of
Technology, Gothenburg, Sweden

Summary

The adverse effect of transient torque reversals (TTRs) on wind turbine gearboxes
can be severe due to their magnitude and rapid occurrence compared to other equipment. The primary damage is caused to the bearings as the bearing loaded zone
rapidly changes its direction. Other components are also affected by TTRs (such as
gear tooth); however, its impact on bearings is the largest. While the occurrence and
severity of TTRs are acknowledged in the industry, there is a lack of academic literature on their initiation, propagation and the associated risk of damage. Furthermore,
in the wide range of operation modes of a wind turbine, it is not known which modes
can lead to TTRs. Further, the interdependence of TTRs on environmental loading
like the wind is also not reported. This paper aims to address these unknowns by
expanding on the understanding of TTRs using a high fidelity numerical model of
an indirect drive wind turbine with a doubly-fed induction generator (DFIG). To this
end, a multibody model of the drivetrain is developed in SIMPACK. The model of
the drivetrain is explicitly coupled to state-of-the-art wind turbine simulator Open-
FAST, and a grid-connected DFIG developed in MATLAB®'s Simulink® allowing a
coupled analysis of the electromechanical system. A metric termed *slip risk duration*
is proposed in this paper to quantify the risk associated with the TTRs. The paper first
investigates a wide range of IEC design load cases to uncover which load cases can
lead to TTRs. It was found that emergency stop and symmetric grid voltage drops can
lead to TTRs. Next, the dependence of the TTRs on inflow wind parameters is investigated using a sensitivity analysis. It was found that the instantaneous wind speed
at the onset of the grid fault or emergency shutdown was the most influential factor
in the *slip risk duration*. The investigation enables the designer to predict the occurrence of TTRs and quantify the associated risk of damage. The paper concludes with
recommendations for utility-scale wind turbines and directions for future research.

KEYWORDS:
Wind Turbine, Transient Torque Reversals, SIMPACK gearbox, Bearing, Voltage Dip, Fault Ride Through

1 | INTRODUCTION

Today, Wind power is one of the most important contributors to cleaner and greener energy drive. In 2020, global new wind
power installations surpassed 90 GW (gigawatt), a 53% growth compared to 2019, bringing total installed capacity to 743
GW, an increase of 14% compared to 2019[1]. New installations in the onshore wind market reached 86.9 GW. The offshore

wind market reached 6.1 GW, making 2020 the highest and the second-highest year in history for new wind installations both onshore and offshore, respectively. In total, 399 GW of onshore wind is projected to be built in 2021-2025[1]. This makes it necessary to develop more robust and resilient wind turbines. One major challenge is reducing downtime occurring from the failure of different parts of the turbine, where gearbox failures typically result in the longest turbine downtime[2]. At the same time, the drivetrain module (gearbox, main shaft, mechanical brake etc.) is only second behind the power module (frequency converter, generator assembly, Low Voltage Switchgear, Medium Voltage Switchgear, transformer etc.) in contribution to the total downtime[2]. It is also important to note that drivetrain module repair costs are typically more expensive due to crane costs. The main contributor to gearbox failures are bearings $\approx$ 70% followed by gears $\approx$ 26% and other failures constitute the rest $\approx$ 4%[2]. 48% of all failures are attributed to high-speed shaft bearings, followed by 13% to the intermediate shaft bearings and 7% to the planetary bearings[2]. All other component failures (gears and others) account for the other 32%. Therefore, it is clear that bearing failures contribute greatly to wind turbine gearboxes' unpredictable and premature failure. Surface damages on high-speed shaft bearings, planetary bearings and intermediate-speed shaft bearings substantially mainly limit the service life[3]. Bearing lives are typically estimated from load ratings made available by the manufacturer and various adjustment factors. It has been observed repeatedly that despite proper user practices by the manufacturer and the end-user, the bearing lives are often limited by wear and damage.

Two prevalent failure modes in multi-megawatt wind turbine gearbox bearings are identified in this paper as smearing/scuffing[4] and white structure flaking (WSF)[5]. Bearings are designed to satisfy a minimum Rolling Contact Fatigue (RFC) life. However, failures within a few years of operation are observed because smearing/scuffing, white etching cracks (WECs), and axial cracking failure modes are different from the classical RCF failure mode. Slip is often considered as being essential to the formation of white etching areas (WEAs)[5], and smearing damage[4]. Slip can independently lead to either smearing/scuffing damage and WSF or severely promote WEA formation[6]. Once an event initiates subsurface WEA formations, normal rolling action of the bearing can initiate cracks at the junction of the inclusion-like areas[7]. The crack inevitably propagates to the surface and becomes a WEC, which grows axially across the raceway and causes premature bearing failures[7]. The slip and impact loading during TTRs is suggested to be a leading candidate in causing stress-induced subsurface WEA damage in[7].

Smearing is defined as the change of the surface area of a metallic roller sliding contact under relative motion due to the beginning of adhesive wear[8]. Cylindrical and spherical roller bearings with large dimensions are especially susceptible to smearing/scuffing due to the sliding and slip conditions within the bearing[9]. According to[8], smearing is connected to the following:

- fast acceleration and deceleration

- fluctuations in slip occurrence

- collapse of the load-carrying lubricant film

- sticking and welding due to material transfer

- high mass moment of inertia of the rolling elements

- light loads

The initiation of smearing has been a topic of much research in the past decades. Although the conditions that lead to smearing are understood, it varies significantly with bearing geometry, lubrication and load fluctuations. Therefore, the existence of one or more of the above-listed conditions does not guarantee to smear. Hamer, et al.[9] used an experimental rig to identify the conditions leading to the onset of smearing. A free-rotating spherical roller was intermittently loaded and unloaded between two inner raceways at a prescribed speed. A clipped sinusoidal loading function is used to simulate loads experienced by a roller in a bearing. The authors noted that scuffing/smearing was not observed if the speed of the roller at the entry to the loaded zone was greater than about 20% of the raceway speed. The authors also identified the collapse of the EHL (elastohydrodynamic lubrication) film due to inlet heating as a possible mechanism that leads to the onset of smearing/scuffing.

Fowell, et al.[10] adapted the original rig of[9]. The authors successfully achieved smearing measured the contact load, roller speed and acceleration, and electrical contact resistance during the tests. The shear stress, friction coefficient, frictional power intensity, and elastohydrodynamic film (EHL) thickness were calculated from the recorded data. The authors concluded that smearing sets in early in the loading phase when the roller is nearly stationary and the frictional power intensity is high.

Scherb and Zech[8] tested a series of INA series cylindrical roller bearings to identify the kinematic behaviour of the bearing and its association to the occurrence of smearing. The authors reported that for loads lower than 1% of the static load limit of

the bearings (C_0), the rollers fail to achieve their kinematic rotational speed leading to slipping and skidding of the rollers. The authors also showed that smearing occurs when the inner raceway speed is higher than 60% of the limiting rotational speed of the bearing, and the applied load had little influence on the condition of smearing.

Selvaraj and Marappan[11] developed a roller bearing test rig to measure the cage and roller slip of a NU 2214 test bearing at different load–speed conditions. They presented their findings on the effect of operating parameters like shaft speed, radial load, lubricating oil viscosity, number of rollers, and bearing temperature on cage slip. Most importantly, the authors concluded that the cage slip is initiated by decreased load, and the magnitude of cage slip is increased with increasing shaft speed.

Evans, et al.[4] performed tests on NU-type cylindrical roller bearings to identify load cases that lead to the occurrence of smearing. The authors performed several tests, including steady-state at with low loads ($\leq 5\%$ of the bearing dynamic load rating, C_1); high and low load with varying speeds; varying lubrication and temperature without being able to achieve smearing successfully. Finally, the authors achieved smearing when the radial load of 1.5% C_1 direction was reversed from the 12 o'clock to the 6 o'clock position. The paper shows that low loads at steady conditions do not result in smearing. However, transient conditions such as rapid reversal of radial load direction aggravate roller slip resulting in smearing.

The second dominant mode of failure often observed in wind turbine bearings is often described as white etching cracks (WECs) and axial cracks and is associated with white structure flaking (WSF)[5]. Axial cracks and WECs associated with the microstructural change in small areas called white etching areas (WEAs) can occur in as little as 6–24 months of operation. They are decorated by white etching areas (WEAs) on the steel surface. White etching refers to the white appearance of the altered microstructure of a polished and etched steel sample. White etching areas around cracks are 10%-50% harder than the surrounding unaffected microstructure. Similar to the phenomenon of smearing, the drivers and mechanisms of their formation are still highly contested. Evans, M. H.[5] presents an extensive review of operational modes, drivers and mechanics that lead to three types of WECs and axial cracks: a) hydrogen-induced, b) electro-thermal stress-induced, and c) mechanical stress-induced. Some of the drivers identified by researchers are hydrogen embrittlement, sliding kinematics, water contamination, low Hertzian contact pressure, electrical potential, lubricant additives, and tensile hoop stress[5,12]. It is clear from the available literature that hydrogen plays a significant role in the embrittlement of the surface, leading to WECs. It has been noted by[12] that WEC initialisation often corresponds to tribological hydrogen generation, and its mechanism is enhanced by sliding kinematics. The authors have also noted that WECs tend to occur at low Hertzian stresses for which high sliding velocities can be reached without prompting quasi-instantaneous damage such as smearing and scuffing. Torrance and Cameron[13] noted that white etching layers were formed in the surface material beneath scuffing damage marks, and Stadler, et al.[6] noted that one of the reasons for steel reaustenization that lead to WEA is smearing/scuffing, thus connecting the mechanism of smearing/scuffing and white etching cracks. Harada, et al.[14] successfully reproduced WEA damage using a disk on roller type rolling contact fatigue test machine and noted that shear stress induced by the slip between the roller and a disk plays an essential role in WEA formation.

The chronological order of events that lead to macroscopic surface failures considered in this paper is schematically depicted in Figure 1. However, it must be noted that the mechanism depicted in Figure 1 does not include all drivers that lead to surface damage; it only includes operational modes that lead to transient torque reversals.
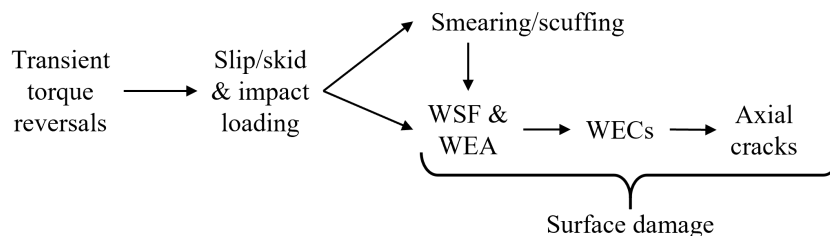

FIGURE 1 Formation of surface damage from transient torque reversals (Note: this diagram only shows the sequence of events that arise from TTRs and does not include all drivers that lead to surface damages in multi-megawatt wind turbine bearings.)

Considerable research has also poured into finding indicators that can warn against the onset of smearing or scuffing of bearings. The indicator that seems to get the most attention is called the Frictional Power Intensity (FPI), defined as $\mu P_{max} \Delta v$ where μ is the friction coefficient, P_{max} is the maximum Hertzian contact pressure (Pa), and Δv is the sliding speed (m/s) between the roller and the inner or outer raceway. Generally, a threshold value is assumed to determine the onset of smearing/scuffing. A

threshold value of 150 MW/m^2 was suggested by Bujoreanu, et al. [15]. The same value was subsequently used by Evans, et al. [4]. Fowell, et al. [10] found that in their experiments, smearing occurred in the range of 105 to 140 MW/m^2 for loads that varies by order of magnitude. Another variable of interest has been the contact temperature that rises. For additive-free mineral oils Kelley, B. [16] suggested contact temperatures of the order of 150°C as the transition point leading to scuffing damage. Fowell, et al. [10] estimated the theoretical maximum contact temperatures of 157°C and 206°C for oil supply temperatures of 17°C and 38°C, respectively. But the predictions vary for different lubricated systems and range from 150°C to 400°C. The onset of smearing can also be tracked by the reduction of lubricant specific film thickness, λ. A drop to $0.6 \leq \lambda \leq 1.6$ from the isothermal value of $1.7 \leq \lambda \leq 4.7$ was reported in [10] as a reasonable indication to the onset of damage. Similar values were also observed by Bowman and Stachowiak [17]. The rise in the lubricant inlet temperature has also been suggested as an important prelude to smearing and scuffing [9,18,19].

Although some indicators like the rise in inlet temperature, rise in FPI etc., have been proposed in the literature that can offer some warning against the onset of smearing/scuffing, the damage onset threshold is highly variable depending on the bearing model and lubrication scheme. They also require a high degree of instrumentation. The required level of instrumentation is rarely available in real-world scenarios. While wind turbine gearboxes are increasingly instrumented, tracking these indicators is very difficult. The other alternative is to identify the load cases that lead to high slip conditions and develop/implement mitigation methods.

Based on the above literature review, the two parameters that mostly dominate smearing/scuffing and WEAs are identified as the bearing loads and raceway speed. A schematic diagram of the risk of cage/roller slip is plotted against bearing loads and raceway speed in Figure 2 to summarise the information available in the literature. It can be observed that the risk of slip increases drastically with decreasing bearing loads and increasing raceway speeds. The load cases that lead to these situations lie outside the range of normal operation. Available industrial reports [7,20] and academic literature [21,22,23] point to the fact that transient events such as emergency shutdown and electrical faults such as grid voltage dips, power converter faults etc., in DFIG based wind turbines lead to rapid variation in electromagnetic torque that can then lead to transient torque reversals in the drivetrain shafts. The following steps are taken to investigate the phenomenon of TTRs in indirect drive wind turbines:

1. Develop a multibody dynamic model of the wind turbine drivetrain in SIMPACK [24] coupled with the state-of-the-art wind turbine simulator OpenFAST [25] and a dynamic model of the DFIG and the associated control systems in Simulink® to obtain a high-fidelity simulation tool capable of predicting transient drivetrain dynamics with a high degree of accuracy.

2. Provide a comprehensive survey of the IEC 61400-1 [26] design load cases to identify the causes that lead to transient torque reversals. The focus is on transient events such as emergency shutdowns and grid faults that can rapidly change the generator's electromagnetic torque.

3. Develop a metric to quantify the risk associated with transient torque reversals that can be used to compare two events and perform a sensitivity analysis.

4. Perform a sensitivity analysis of TTRs to inflow wind parameters to identify the impact of site-specific wind flow parameters on the risk of damage associated with transient torque reversals.

The paper is structured as follows: first, the model used for numerical investigation is detailed in Section 2. Then the metric *slip risk duration* quantifying the risk associated with TTRs is derived based on the available literature is introduced in Section 3. Thereafter, IEC 61400-1 [26] the design load cases investigated for TTRs are introduced in Section 4. Section 5 presents the results of this paper. First, the load cases that lead to TTRs are discussed, followed by the propagation of the TTRs (induced by the transient events) from the high-speed shaft to the main shaft of the drivetrain. The section then presents a sensitivity analysis of the risk associated with transient torque reversals to inflow wind parameters. Section 5 is concluded with a case study of a mid-western Swedish wind farm. The paper ends with some considerations for multi-megawatt DFIG wind turbines and suggestions for future research.

2 | GENERIC MODEL OF A 2 MW ONSHORE WIND TURBINE

A generic 2 MW wind turbine model is developed to mimic the behaviour/power production of a Vestas V90 machine. The generic turbine has a cut-in wind speed of 3.5 m/s, reaches its maximum power at 12 m/s and automatically shuts down if the hub-height wind speed is higher than 25 m/s. The state-of-the-art aeroelastic simulation tool OpenFAST [25] is used for aeroelastic
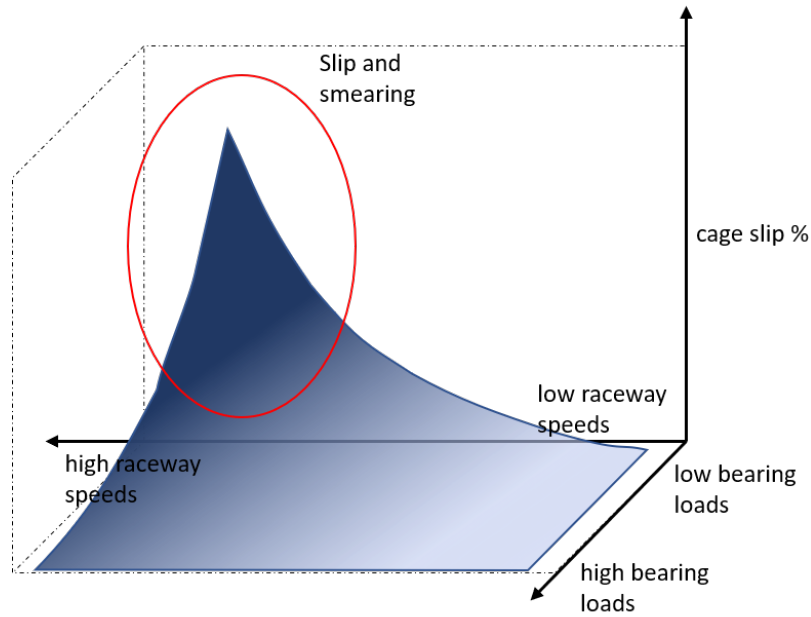
FIGURE 2 Schematic diagram: region of expected sliping and smearing

simulations of the wind turbine in this paper. The generic 2 MW wind turbine model is developed by down-scaling the NREL 5 MW reference wind turbine[27] guided by Vestas V90-2.0[28] power curve and the available SCADA data. The 2 MW wind turbine specifications used in this paper are summarised in Table A1. It must be noted that the generic 2 MW wind turbine model used here is not aimed to be an exact representation of a Vestas V90 wind turbine but serves as a baseline 2 MW wind turbine model that mimics the performance of a Vestas V90-2.0[28] turbine.

The coupled numerical model developed in this paper comprises a multibody dynamic model of the wind turbine drivetrain developed in SIMPACK, a dynamic model of the DFIG and the associated control systems developed in Simulink®. Furthermore, these two models are coupled with the wind turbine simulator OpenFAST to offer a high fidelity numerical model of the coupled electromechanical system. The models are briefed in the following.

2.1 | Multibody drivetrain model in SIMPACK

A model of the drivetrain has been developed using the multibody system simulation software SIMPACK[24]. The four-point drivetrain is a three-stage gearbox with one planetary stage and two helical stages. The main shaft is supported by two spherical bearings, and the high-speed shaft is supported by three bearings are shown in Figure 3. The main bearings are connected directly to the bedplate, whereas all other bearings are connected to the gearbox housing. The downwind end of the high-speed shaft is connected directly to the generators. Figure 4 shows the drivetrain model developed in SIMPACK. The structural members of the drivetrain are modelled as rigid bodies. All gears are modelled using the primitive `25: Gear Wheel` from the SIMPACK library using the data presented in Table A2. The SIMPACK Force Element `225: Gear Pair` is used for a detailed description of all tooth contact between two meshing gear wheels with involute geometry. The `225: Gear Pair` element allows multiple tooth meshing, whereby all the individual tooth pairing contacts along the line of action are calculated. The resulting overall transfer forces and torques are calculated by adding the individual forces at each contacting tooth. The `225: Gear Pair` element is capable of estimating the time-varying meshing forces between two gear wheels. The shaft(s) flexibility is modelled using the SIMPACK Force Element `43: Bushing Cmp` in SIMPACK. In this study, the torsional stiffness of the shafts is used. The bearings are modelled using Force Element `88: Rolling Bearing` in SIMPACK with the data presented in Table A3.
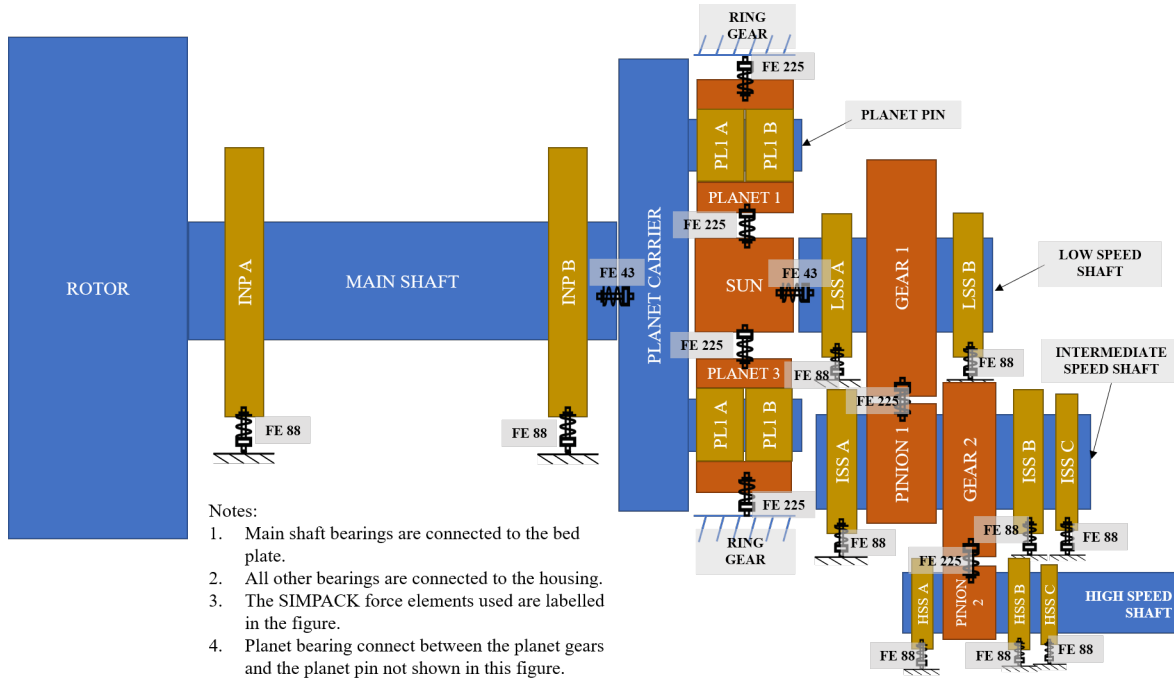
FIGURE 3 Schematic model of the drivetrain

2.2 | Generic 2MW Doubly-Fed Induction Generator

This section provides a brief description of the grid connected Double-Fed Induction Generator (DFIG) and the associated rotor side and grid side control. The generator is modelled using the `Asynchronous Machine SI Units` block in Simulink®. The generator parameters are provided in Table A4. The stator is connected directly to the grid (the transformer is ignored), and the rotor is connected through the back-to-back AC/DC/AC converter. The grid is modelled using a `Three-Phase Programmable Voltage Source` Simulink® block, and the mechanical speed Ω_m of the shaft is obtained from the SIMPACK model and is assumed to be equal to the high-speed shaft velocity at the generator end. A majority of the blocks used to develop the grid-connected DFIG model are provided by the Simscape™ Electrical™ Specialized Power Systems library. The `powergui` is an environment block that contains the equivalent Simulink® circuit that represents the state-space equations of the models in the Simscape Electrical Specialized Power Systems library.

2.2.1 | Vector control of DFIG using an AC/DC/AC converter

The rotor-side converter (RSC) and the grid-side converter (GSC) controller are modelled in the *dq* reference frame where the *d*-axis is aligned with the stator flux space vector. Due to this orientation, at the RSC, direct rotor current control is analogous to stator reactive power control, and quadrature rotor current control is analogous to stator active power control or electromagnetic torque control. At the GSC, direct grid current control is analogous to DC bus voltage control and quadrature grid current control is analogous to grid reactive current control.

Control of RSC

The rotor side controller has a cascading structure with two control loops. The outer loop controls the stator's active and reactive power, and the inner loop controls the rotor's direct and quadrature currents. As noted previous, the *dq*-frame separates the two outputs and hence, the torque/active power can be controlled independently using the *q* rotor current and the reactive power can be controlled independently by the *d* rotor current. In this paper, active and reactive power references are not used, thus eliminating the outer loops. Instead, during normal operation, i_{dr} (direct rotor current) is set to zero, minimising reactive current; and, *indirect speed control* method is used to set the reference electromagnetic torque based on the mechanical rotor speed. The reference and the measured rotor currents are then fed to two independent PI (proportional-integral) controllers to determine the reference rotor voltage. Finally, the reference rotor voltage is sent to the `PWM Generator (2-Level)` Simulink® block to
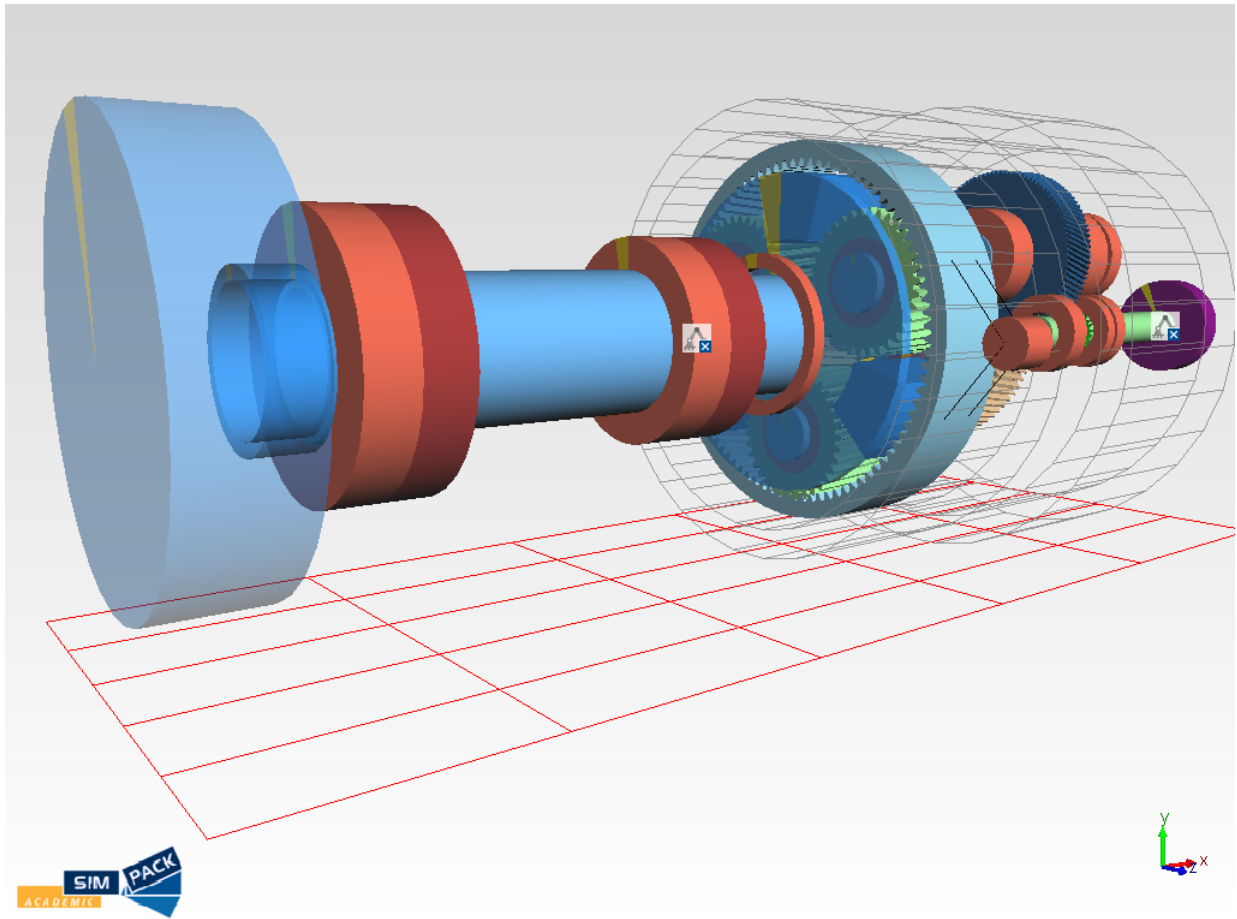
FIGURE 4 SIMPACK model of the drivetrain

generated switching signals for a 2-Level Voltage Source Converter (VSC) modelled in Simulink® using an `Universal Bridge` block. The control architecture is shown in Figure 5b.

Control of GSC

The GSC controller is designed to control power flow through the rotor to the grid and the DC bus voltage of the back-to-back converter. The GSC controller also has a cascading structure similar to the RSC controller. Again, the *dq*-frame separates the control of the DC bus voltage and reactive power delivered to the grid. The DC bus voltage and the reactive power delivered at the grid can be controlled independently using the direct and quadrature grid currents, respectively. The DC bus voltage controller, typically a PI controller, is used to determine the reference grid direct current. The reactive power delivered at the grid can be set to zero, therefore rendering the reference quadrature grid current zero. However, the reactive grid power can be set to a reference value based on grid code requirements. The obtained reference signals and measured signals of the grid direct and quadrature currents are sent to two independent PI controllers to obtain the reference filter voltage. Similar to the RSC, the reference voltage signal is sent to a `PWM Generator (2-Level)` Simulink® block to generate switching commands for a 2-Level VSC. The control architecture is shown in Figure 5c.

2.2.2 | Performance during severe grid voltage dips

When a grid voltage dip is seen directly by the stator, the rotor voltage should simultaneously and significantly increase to prevent high rotor currents. However, due to the dimensioning of the converter, it can only provide the rotor with voltages of approximately 1/3 of the stator voltage. Due to the slow evolution of stator flux and the rotor voltage limitation, the DFIG is unable to maintain rotor currents below the safe limits without losing control[29]. Crowbar protection is activated to accelerate

flux evolution while simultaneously recovering converter control as quickly as possible to solve these problems imposed by the voltage dips.

As demanded by grid codes, to provide Low Voltage Ride Through (LVRT) capabilities, the wind turbine must remain connected during the voltage dip while providing reactive power through the stator. The step undertaken during a severe voltage dip in this paper are as follows:

1. Initially, the DFIG operates at a speed determined by inflow wind speed.

2. When the voltage dip occurs, it is detected by a rise in rotor current. However, this detection takes a few milliseconds (typically 0.5-5 milliseconds), and during this period, the system cannot guarantee control.

3. On detecting the voltage dip, the crowbar is activated to demagnetise the machine. While the crowbar is open, the converter is inhibited to protect it from overcurrent. The crowbar activation duration depends on the machine design. In this paper, the crowbar is activated for 100 milliseconds.

4. Once the flux has decayed, the crowbar is deactivated, and control is restored to the rotor converter. For the remaining duration of the fault, the entire rotor current is used to provide reactive power by setting d-current to the rated rotor current.

5. Once the voltage is recovered, normal operation is resumed.

2.3 | Coupling the drivetrain and generator models with OpenFAST

(a) Coupling OpenFAST, SIMPACK and DFIG

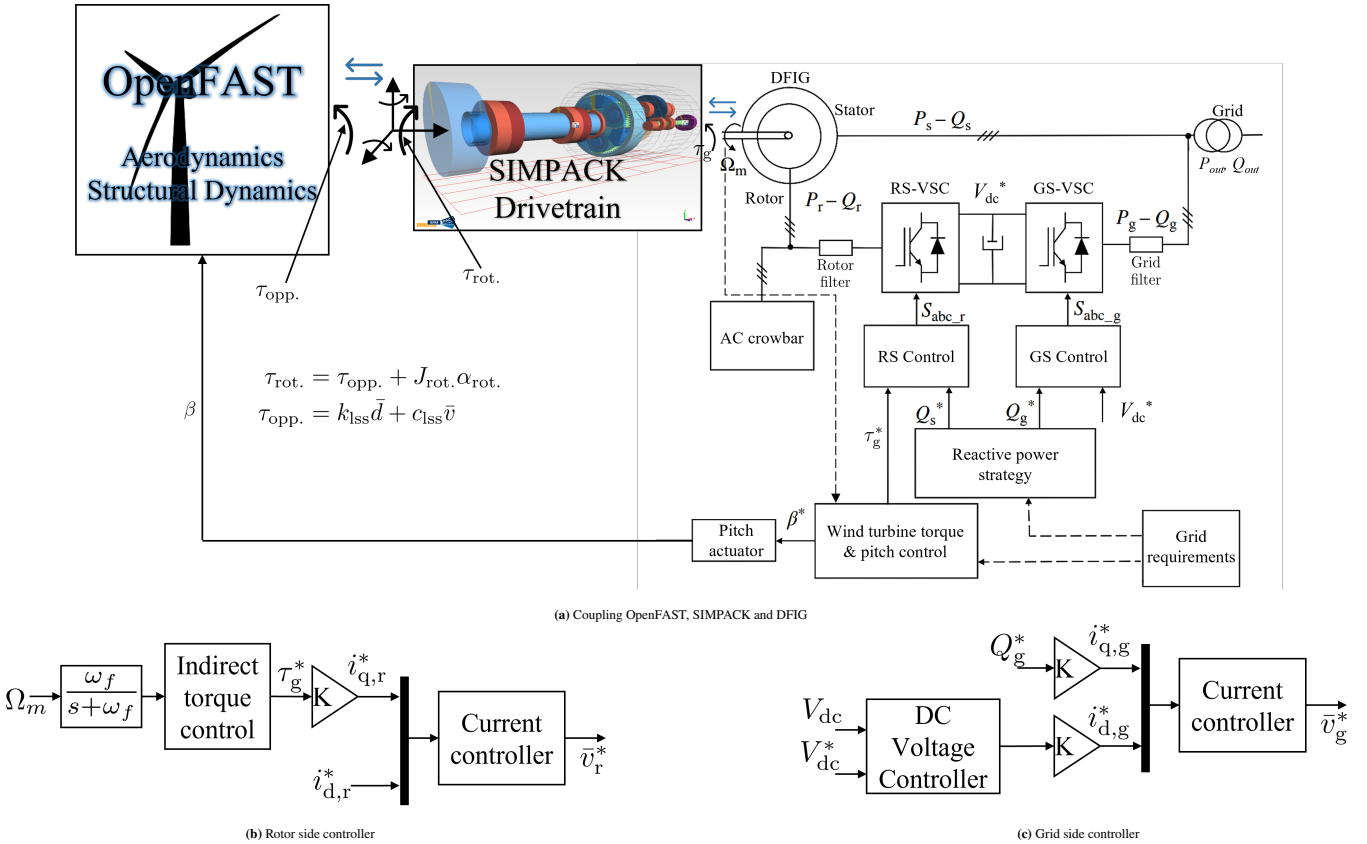**(b)** Rotor side controller

(c) Grid side controller

FIGURE 5 Coupled OpenFAST, SIMPACK, DFIG and associated control systems

As described in the previous sections, the wind turbine is modelled in the open-source software OpenFAST[30], and the drivetrain is modelled in SIMPACK[24], and the grid-connected DFIG is modelled in Simulink®. Therefore, the three models must be

externally coupled. In this paper, the three models are coupled in Simulink®. OpenFAST offers an interface to Simulink® implemented as a `Level-2 S-Function` called `FAST S-Function`. The interface is written in C, and it calls a DLL of OpenFAST routines, which are written in FORTRAN. On the other hand, SIMPACK provides a co-simulation interface between SIMPACK and MATLAB® Simulink® called SIMAT. Using SIMAT, the two co-simulation partners exchange their results with a given time step using the TCP/IP protocol. This allows the user to take direct advantage of the complex mechanical systems modelled in SIMPACK and the control systems designed in Simulink®. The coupling mechanism adopted in this paper is motivated by the results presented in[31]. In this mechanism, the drivetrain torsional model in OpenFAST is turned off, and the gearbox ratio is set to 1. The resulting opposing torque is measured at the low-speed shaft and used in place of the opposing generator torque. The SIMPACK model, at the rotor end, accepts the three-dimensional rotor torques/moments and transverse forces. The force transfer is depicted graphically in Figure 5a. As mentioned in the previous section, the 2 MW DFIG model is developed in Simulink® and solved in discrete time using the `powergui` environment block. Zeroth order hold is used in Simulink® to connect the continuous and discrete-time systems. The coupled system in Simulink® and the associated control systems are shown in Figure 5.

3 | A METRIC TO QUANTIFY TTRS

While the wind energy community acknowledges transient torque reversals (TTRs) as a phenomenon, no known method quantifies the severity of the TTRs arising from different events. Therefore, a metric is needed that can offer a quantitative understanding of the severity of the TTRs. One natural idea is to count the number of zero crossings by the radial bearing load or the radial bearing loading angle. In this approach, one could quantify the severity of a TTR by the number of zero-crossing. However, it has been shown in experimental studies that while TTRs amplify the risk of smearing/scuffing, they can occur even without rapid reversal of the loading angle. Therefore, in this paper, a quantity termed as *slip risk duration* is proposed. The *slip risk duration* represents the duration spent by the bearings in a high slip risk situation. The metric is formulated by defining thresholds crossing, resulting in an increased slip risk. From the reviewed literature, the two important thresholds are identified as: a) a critical radial bearing load, below which it can be considered that the bearings are *lightly loaded*, and b) a critical inner-raceway speed, above which the shaft is *rotating fast*. Ideally, to formulate these thresholds, the bearing at hand must be tested using the appropriate choice of lubricant and temperature. In the lack of such experimental results, these thresholds are determined from the reviewed literature. The various bearings tested by different researchers are compared with the gearbox bearings considered in this paper and are summarised in Table 1. Table 1 shows the inner-raceway speed at which slip was first observed in different experimental studies. The table also specifies the threshold speed assumed in this paper. It can be observed that the bearings found in the literature are dimensionally comparable to the HSS-A and the ISS-A cylindrical bearings used in this paper. The LSS-A spherical bearing, on the other hand, is larger. Therefore, if the same raceway velocity and bearing load are applied to all the bearings, the larger LSS-A bearing is more susceptible to slip induced damage (smearing/scuffing or WSF)[9]. Based on the derived knowledge from literature, the following thresholds have been assumed in this paper.

1. Low radial bearing forces $\leq$ 1% C (dynamic load rating) accompanied by the sporadic and rapid reversal of radial load direction.

2. Simultaneously, the inner-raceway speed must be higher than 2.6 m/s.

The above two criteria are used to estimate the *slip risk duration*. The time spent is used as the metric to study the risk of slipping/smearing associated with the different load cases in the following.

4 | LOAD CASES INVESTIGATED FOR TRANSIENT TORQUE REVERSALS

The design load cases covering the life of a wind turbine can be represented by a set of design situations covering the most significant conditions that the wind turbine may experience. The load cases are determined by combining various operational modes and design situations, such as specific assembly, erection or maintenance conditions, with the external conditions. The IEC 61400-1[26] categorises the required design load cases into Fatigue "F" and Ultimate "U" load cases. While fatigue load cases include normal operating scenarios, the ultimate load cases are subdivided into normal "N", abnormal "A" and transportation

Parameters	Scherb and Zech [8] NJ 2332 C3	Evans et al. [4] NU-type CRB	Fowell et al. [10] SRB 23230 roller	HSS-A NU 2234	ISS-A NU 2338	LSS-A 23984 CC
d (mm)	160	160	150	170	190	420
D (mm)	340	290	270	310	400	560
B (mm)	114	98.425	96	86	132	106
C_1 (kN)	1250	–	1129	1060	1830	2083
C_0 (kN)	1730	–	1460	1340	2550	4150
Inner-raceway speed (m/s)	3.2 [8]	18.2 [4]	2.6 [10]	2.6	2.6	2.6
Comment	rotational velocity sweep; speed at which slip first observed	fixed rotational speed; radial load direction reversal; slip & smearing	rotational velocity sweep; limiting speed at which smearing observed	assumed	assumed	assumed; slip can occur at a lower velocity due to large size

TABLE 1 Bearing ratings literature vs this paper

and erection "T". Due to the transient nature of the TTRs, it is assumed that TTRs will be observed in the "U" load cases. Further, this paper focuses on two types of load cases chosen as

1. Normal Ultimate load cases that are expected to occur frequently within the lifetime of a wind turbine, like, control system or electrical network fault, emergency shutdown, and parked/idling situations.

2. Abnormal Ultimate load cases that are less likely to occur, like extreme operating gust coupled with electrical network fault, parked/idling turbine at extreme wind speed coupled with electrical fault etc.

The load cases from IEC 61400-1 [26] considered in this paper are summarised in Table 2.

5 | RESULTS AND DISCUSSION

This section is organised as follows: First, the developed SIMPACK-DFIG model and the external coupling are compared against the baseline OpenFAST model to prove its validity. Next, a discussion is presented on the cases that are identified to induce TTRs. The next section presents a sensitivity analysis of the proposed *slip risk duration* to the inflow wind parameters. This section is concluded with the case study of a mid-western Swedish wind farm.

5.1 | Verification of the coupled OpenFAST-SIMPACK-DFIG model

To verify the developed coupled OpenFAST-SIMPACK-DFIG coupled model, a code-to-code comparison of the coupled system against the baseline OpenFAST [30] model is presented in Figure 6 and 7. As mentioned in Section 2 all simulations are performed using the developed Generic 2MW turbine. The input full-field wind files are generated using TurbSim [32], and the turbine is operated using a variable speed torque control and full span collective blade pitch control. The predicted rotor and generator speeds and high-speed shaft and main-shaft torques obtained from the two models are compared. Figure 6 compares the prediction obtained from the two models during normal operation. It can be observed that the two models match well. In a second case, the prediction from the two models is compared in Figure 7 during an emergency shutdown. The emergency shutdown mechanism employed in this paper uses aerodynamics braking common to all modern pitch regulated wind turbines [33]. A qualitative comparison of the high-speed shaft torques of 2 MW wind turbine during an emergency shutdown between the numerical models in Figure 7c and the measurements presented in [7] show that the predictions obtained from the coupled OpenFAST-SIMPACK-DFIG model match better than the baseline OpenFAST model in capturing the fundamental torsional oscillations. Therefore, the

DLC	Situation	Assessment	Simulation setup							Occurrence of TTRs
			Length (s)	Wind (m/s)	Yaw	Turbulence	Shear (α)	Gust	Fault description	
2.1	Power production + Grid fault	Extreme - normal event	25	12	0°	NTM	Vertical; 0.2	None	90% symmetrical voltage dip @ 15 s	Yes
2.2 a	Power production + Pitch system fault	Extreme - abnormal event	50	12	0°	NTM	Vertical; 0.2	None	One blade operating at minimum pitch angle	No
2.2 b	Power production + Pitch system fault	Extreme - abnormal event	50	12	0°	NTM	Vertical; 0.2	None	@ 25 s collective pitching towards minimum pitch angle at the maximum pitch speed	No
2.2 c	Power production + Yaw system fault	Extreme - abnormal event	50	12	15° to 345° with steps of 15°	NTM	Vertical; 0.2	None	Yaw system fault	No
2.3	Power production in EOG + Grid fault	Extreme - abnormal event	25	25	0°	None	Vertical; 0.2	EOG: Equation (17) [ref]	90% symmetrical voltage dip @ 15 s	Yes
3.2	Start up during EOG	Extreme - normal event	50	25	0°	None	Vertical; 0.2	EOG: Equation (17) [ref]	None	No
3.3	Start up during EDC	Extreme - normal event	50	25	0°	None	Vertical; 0.2	ECD: Equation (21) [ref]	None	No
4.2	Shut down during EOG	Extreme - normal event	50	25	0°	None	Vertical; 0.2	EOG: Equation (17) [ref]	None	No
5.1	Emergency shut down	Extreme - normal event	50	25	0°	NTM	Vertical; 0.2	None	shutdown @ 25 s; without mechanical brake	Yes
6.2	Parked 50-year extreme wind + loss of electrical network	Extreme - abnormal event	50	V50	300°	11%	Vertical; 0.11	None	abnormal yaw error due to loss of electrical network connection	Yes
6.3	Parked 1-year extreme wind + yaw system error	Extreme - normal event	50	V1	20°	11%	Vertical; 0.11	None	idling rotor with yaw system fault	Yes

TABLE 2 Load cases

coupled OpenFAST-SIMPACK-DFIG model can replicate the dynamics of the baseline OpenFAST model during normal operation. The coupled model is also more realistic than the baseline OpenFAST model in predicting transient drivetrain dynamics. All subsequent analysis is performed using the coupled OpenFAST-SIMPACK-DFIG setup.
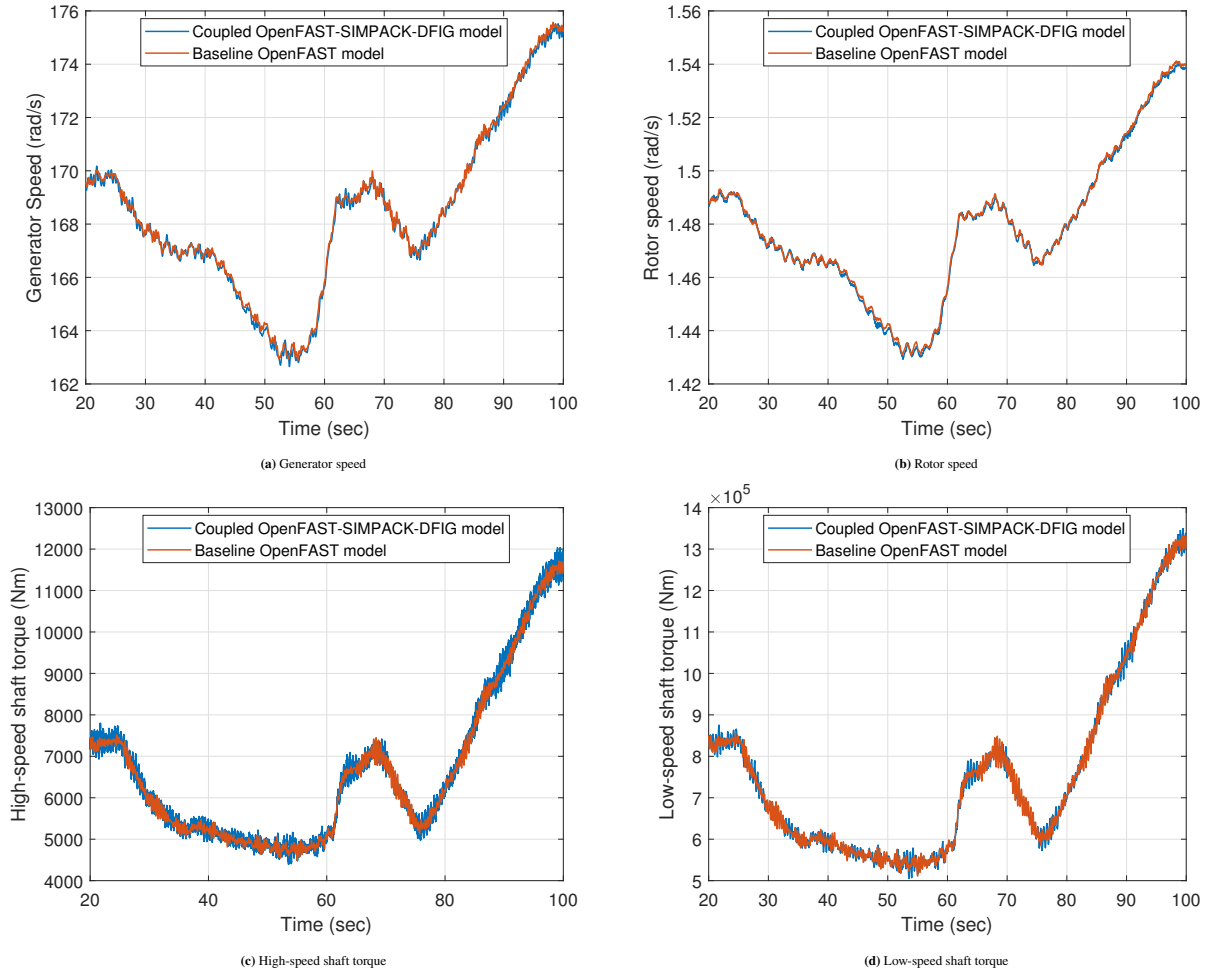
(a) Generator speed

(b) Rotor speed

(c) High-speed shaft torque

(d) Low-speed shaft torque

FIGURE 6 Model verification results – normal operation

5.2 | Load cases that initiate TTRs

Numerical investigation into the load cases presented in Table 2 showed that not all of the load cases considered herein induced TTRs, creating a high slip risk situation. TTRs is induced when there is a rapid fluctuation in the generator (electromagnetic) torque. This includes cases such as a) electrical grid faults (DLC 2.1 & 2.3), where torque control is lost momentarily, b) emergency shutdowns (DLC 5.1), where the generator is reduced with a high gradient, and c) parked/idling cases (DLC 6.2 & 6.3) when the generator is disconnected, and the mechanical brake is not deployed. From here on, the analysis is focused on cases a) and b) as it can be assumed that the stationary condition during idling will not lead to a high slip risk condition. Figure 8a shows the high-speed shaft torque and speed followed by the HSS-A radial bearing force and the loading angle in Figure 8b for DLC 2.1 (power production + grid fault). It can be observed that during the fault, the high-speed shaft experiences multiple torque reversals, and the radial forces in the HSS-A bearing drops substantially while its direction changes sign rapidly. Similar behaviour is observed during an emergency shutdown event (DLC 5.1) in Figure 9. During the emergency shutdown, the sudden drop in electromagnetic torque leads to multiple torque reversals in the high-speed shaft that are accompanied by a rapid reversal in bearing load direction.
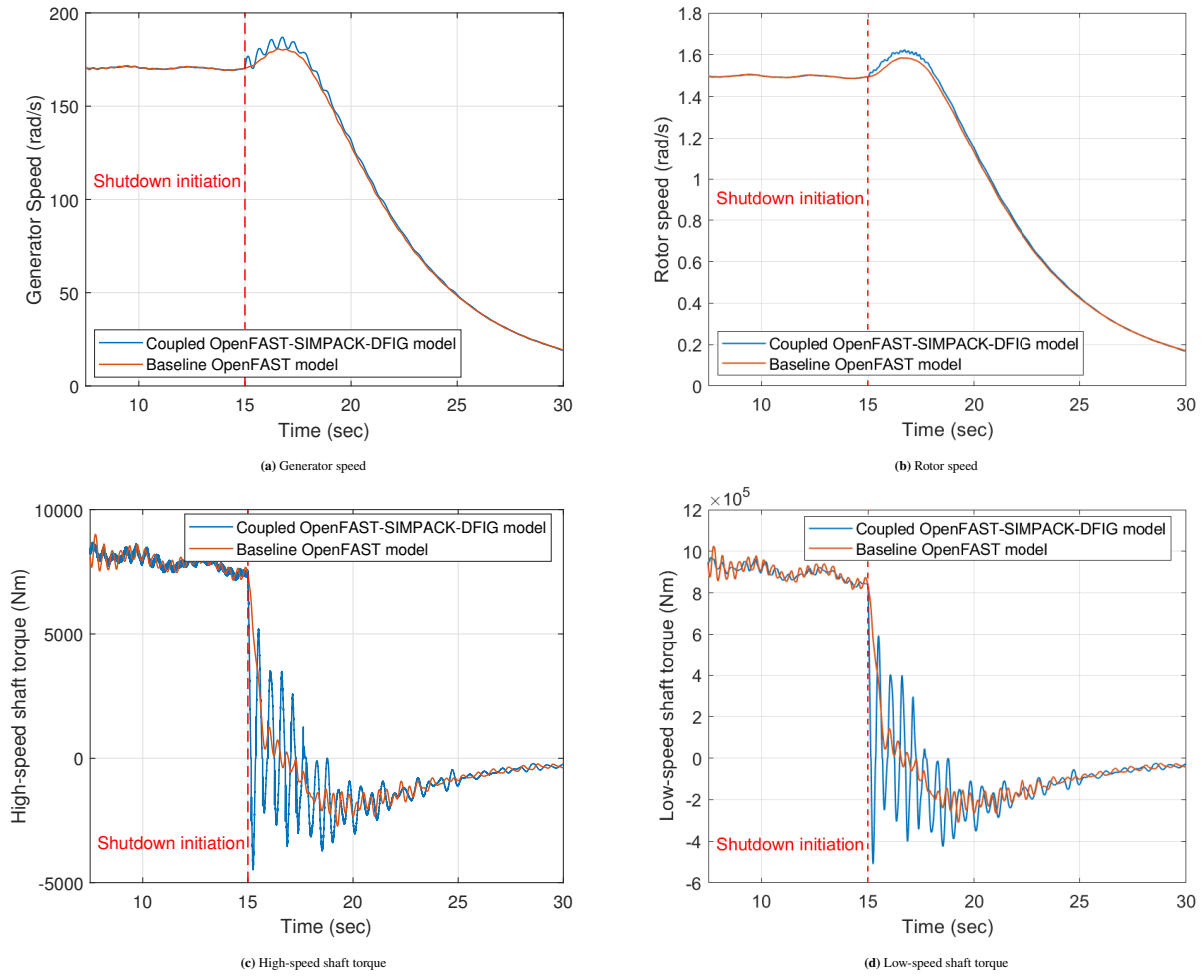
(a) Generator speed

(b) Rotor speed

(c) High-speed shaft torque

(d) Low-speed shaft torque

FIGURE 7 Model verification results – emergency shutdown

(a) HSS torque and speed

(b) HSS-A radial force and angle
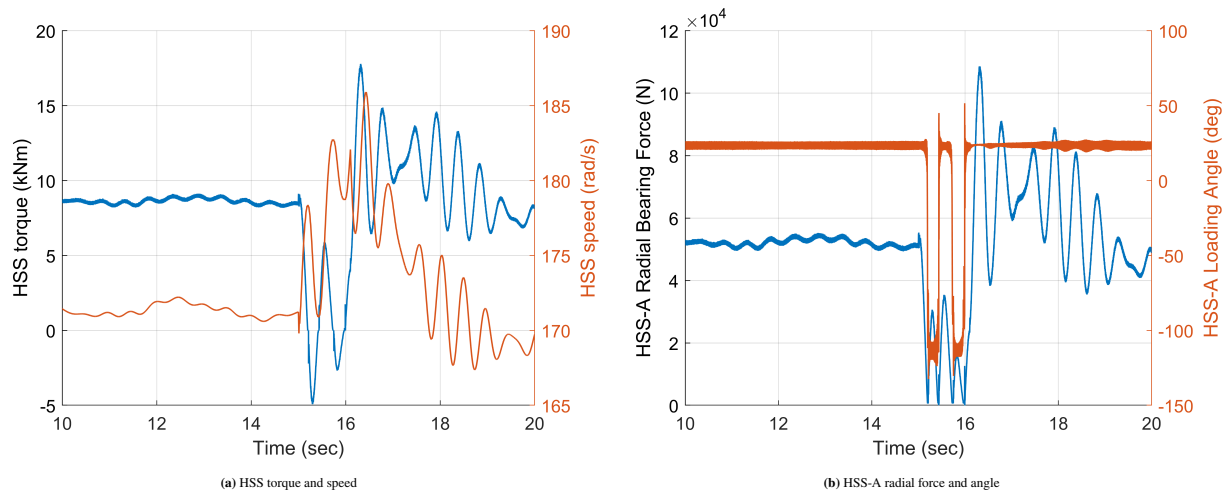
FIGURE 8 Initiation of TTRs during voltage dips

(a) HSS torque and speed

(b) HSS-A radial force and angle
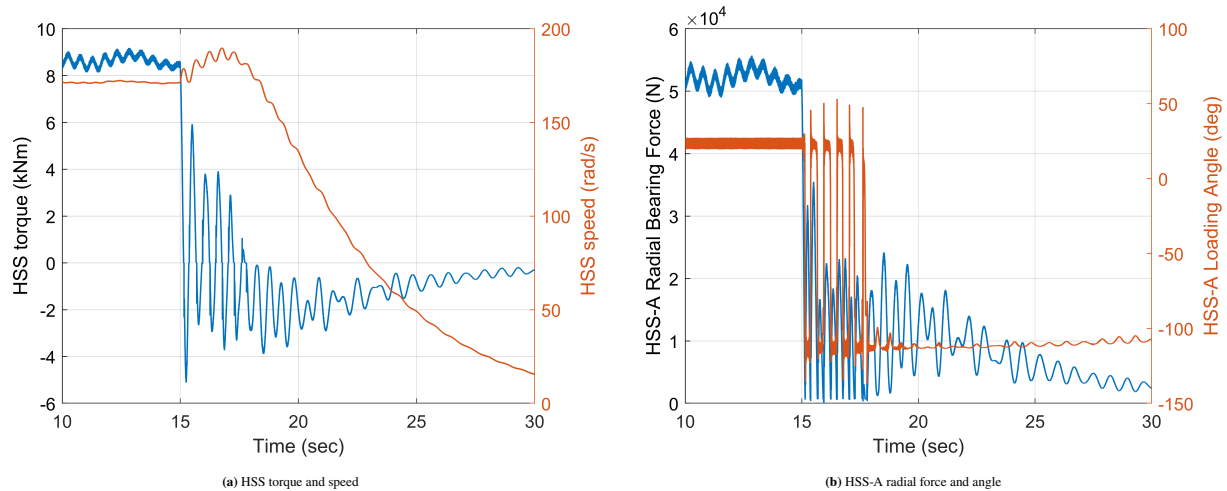
FIGURE 9 Initiation of TTRs during emergency shutdown

5.3 | Fault propagation through the drivetrain

Before quantifying the damage risk associated with the TTRs, it is important to investigate how the TTRs propagate through the drivetrain from the high-speed shaft to the main shaft. To investigate the propagation of the TTRs, DLC 2.1 is considered in this section. However, the analysis is also valid for the other DLCs that have been identified to induce TTRs in the previous section.

In DLC 2.1, the electrical fault occurs at the grid, resulting in a symmetric voltage drop. This drop increases the rotor current triggering the crowbar to open and inhibits the converter resulting in a loss of control. The most representative magnitudes of the 2MW DFIG affected by the 90% voltage dip simulated in DLC 2.1 are shown in Figure 10. In the simulation, the fault occurs at 15 seconds, lasts for 500 milliseconds, and the recovery starts at 15.5 seconds. It can be observed that right after the fault, the crowbar current shoots up and the crowbar is kept open for 100 milliseconds, and there is transience in the DC bus voltage. The rotor side converter is hindered as long as the crowbar is open. After 100 milliseconds, the crowbar is disconnected, and control is returned to the RSC. However, until complete recovery at 16.1 seconds, the entire stator current is directed to provide reactive power, and the torque control is lost for the entire fault duration of 1.1 seconds (15–16.1 seconds). It must be noted that the grid fault configuration assumed here is designed to simulate a worst-case scenario. If measures are taken to maintain rotor side control during the fault, or if the requirement of reactive current through the stator is only a fraction of the total current, some of the damaging transience caused by the loss of torque control can be alleviated.

However, it can be observed here that the sudden loss of electromagnetic torque results in TTRs that propagates through the drivetrain. The Figures 11 and 12 show the propagation of the fault. The results show the radial bearing forces on the different bearings and the corresponding loading angle. At 15 sec, at the occurrence of the fault, the radial forces drop suddenly and significantly, accompanied by a rapid reversal in the loading angle. The fault results in a small time window of high slip/smearing risk. It can be observed in Figures 11 and 12 that the TTRs travel until the planet bearings. The TTRs are, however, not dominant in the planet-carrier bearings and the main-shaft bearings in Figure 12 respectively, due to the self-weight of the shafts and the gearing elements. While the fault can be easily identified in the dynamics of the planet-carrier and main-shaft bearings, its magnitude is not large enough to reverse the loading angle. Therefore, these bearings can be considered safe from the point of view of TTRs.

The criterion set on the inner-raceway speed set in Section 3 translates to a rotational speed of 25.4, 21.7 and 11.2 rad/s for the high-speed shaft, intermediate-speed shaft and the low-speed shaft, respectively. While the numerical investigation includes all shafts and bearings, the results are limited to the high-speed shaft bearings only as it is found that the trends and the qualitative description of the impact of the transient events are the same as all other upwind bearings, as shown in Figure 11. Therefore, from here onward, the discussion is limited to high-speed shaft bearings only. Figures 13 through 15 show the high-speed shaft rotational speed, HSS-A radial bearing load and HSS-A radial bearing load angle for hub height mean wind speeds of 11 m/s, 6 m/s and 4 m/s, respectively. The Figures 13a, 14a and 15a show that high-speed shaft speed is always above the threshold, including the duration of the fault, therefore satisfying criterion number 2. While criterion number 1 is satisfied only during the duration of the fault as observable in Figure 13b, 14b and 15b. The time of the fault is marked as "critical time" in the figures.
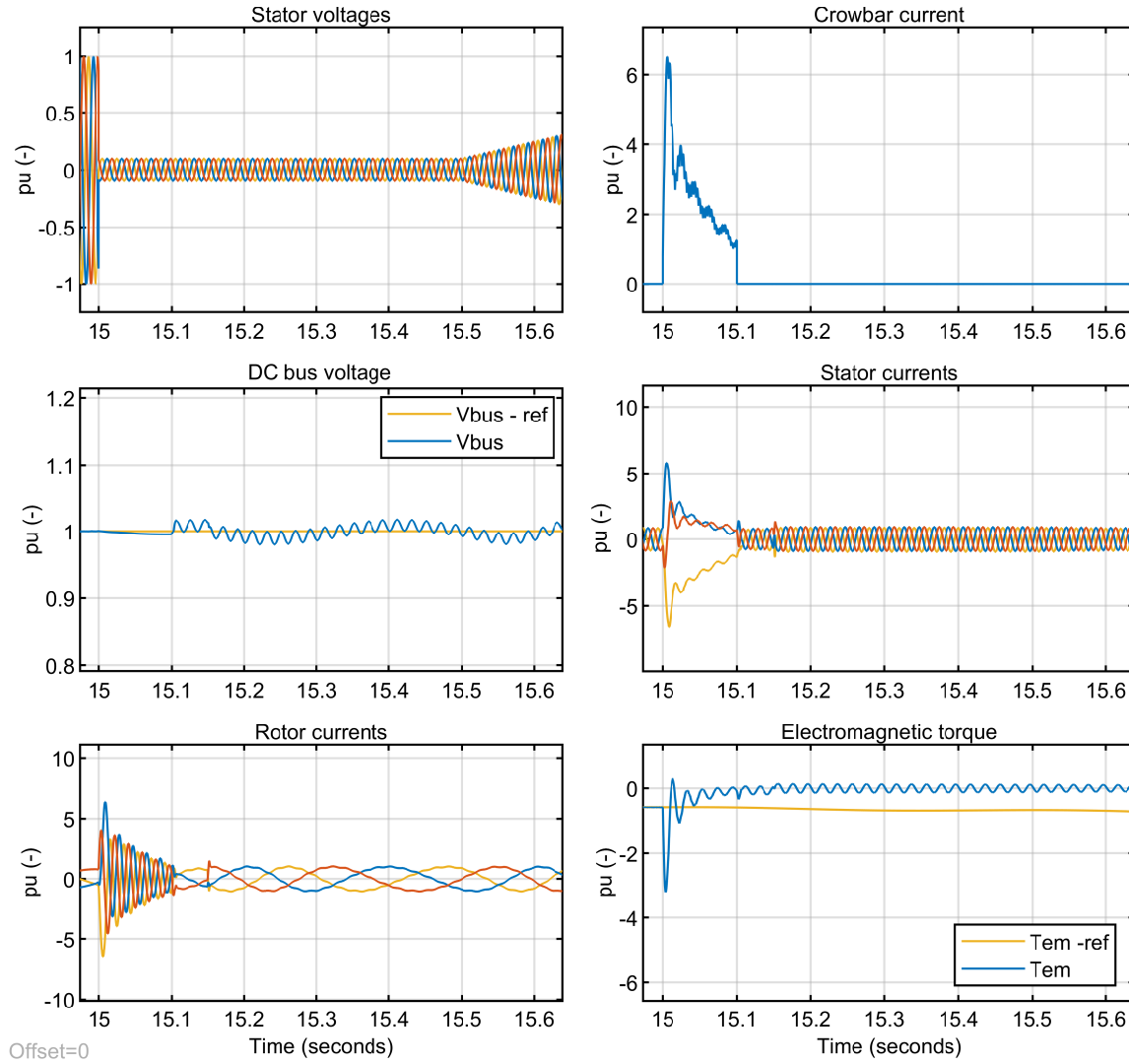
FIGURE 10 Most representative magnitude of a 2 MW DFIG base wind turbine affected by a symmetric voltage drop of 90% seen directly by the stator.

It is important to note that the proposed metric *slip risk duration* is a subset of this "critical time". The *slip risk duration* is the "critical time" when the radial bearing load is below $\leq$ 1% of its dynamic load rating. It also is worth noting that in Figure 15a the bearing load is lower than the threshold for the entire simulation. However, the entire operating condition at wind speeds of 4 m/s has not been deemed *slip risk* due to the absence of rapid reversals in radial loading direction at times other than the duration of the fault. It is important to note from Figure 13b, 14b and 15b that the "critical time" and therefore the *slip risk duration* increases with decreasing wind speeds, showing that the *slip risk duration* induced by the electrical fault is dependent on the inflow wind. With this in mind, the impact of inflow wind parameters on the risk of induced damage is investigated in the next subsection.

5.4 | Sensitivity of TTRs to inflow wind parameters

In this section, the impact of inflow wind parameters on the slip risk duration induced by the occurrence of TTRs is investigated. The inflow wind parameters considered here are: a) hub-height mean wind speeds, b) turbulence intensity, c) vertical shear, and d) wind veer (vertical uptilt angle). In[34], the authors investigated the sensitivity of 18 wind inflow parameters on the structural loads of a wind turbine. The choice of parameters in this paper is inspired by selecting the parameters that had the maximum
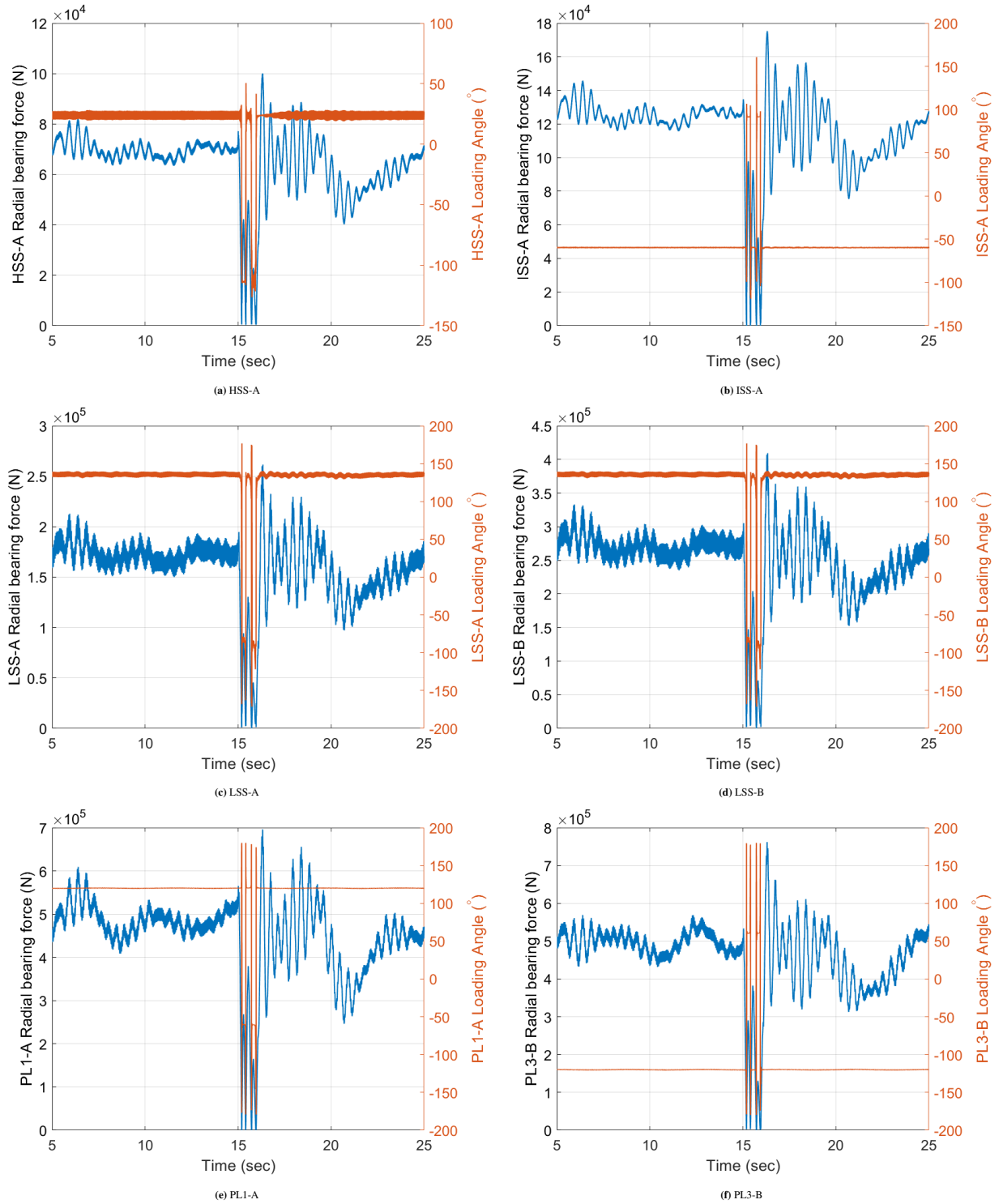
FIGURE 11 High-speed shaft, low-speed shaft and planet bearings

impact on the rotor torque or main shaft bending moments in[34]. The metric *slip risk duration* defined in Section 3 is used to quantify the sensitivity. The spatially coherent full-field wind files are created using TurbSim[32]. For every realisation of the chosen parameter set, ten random seeds to account for the stochastic nature of the underlying Kaimal spectrum are used to generate the time histories.
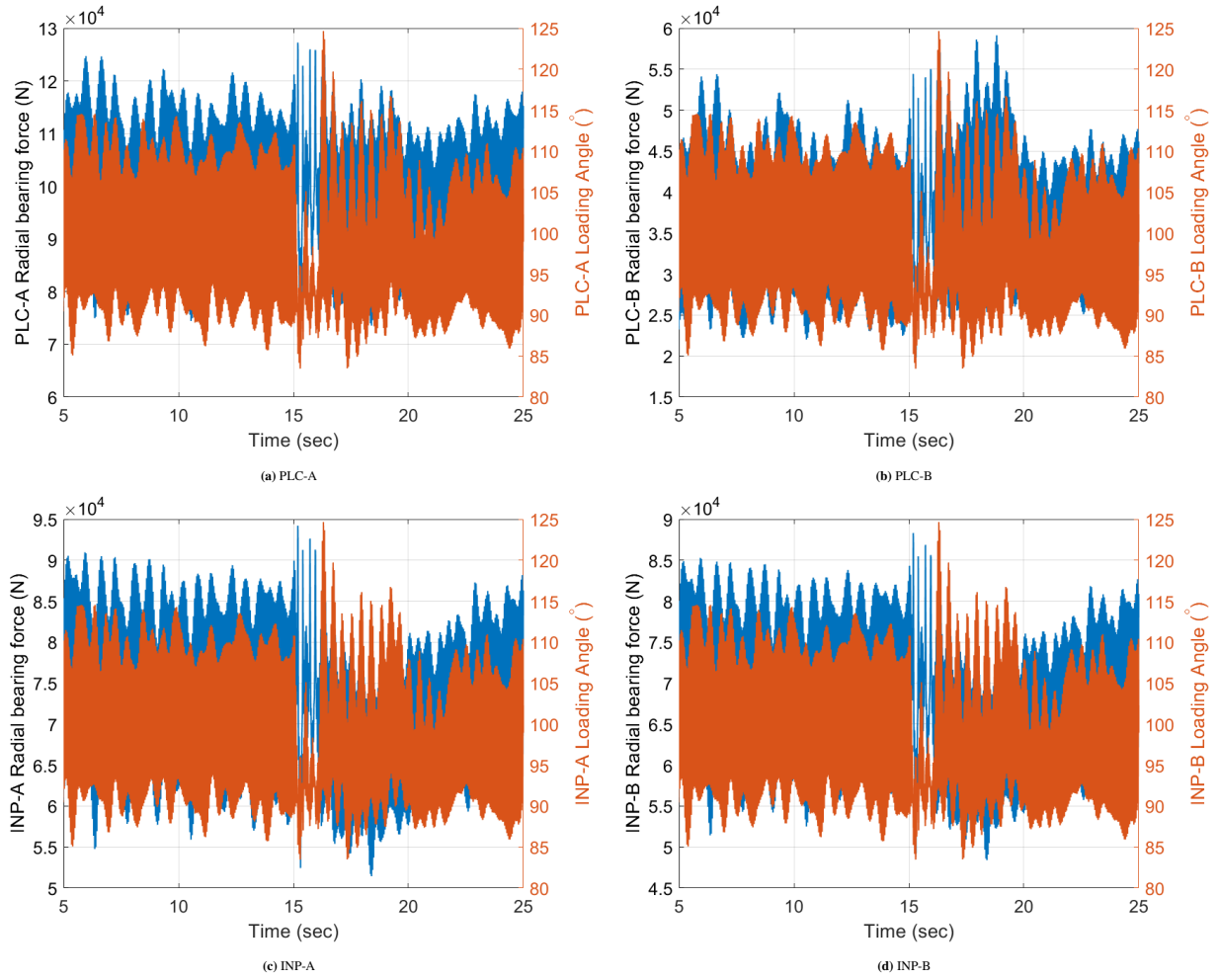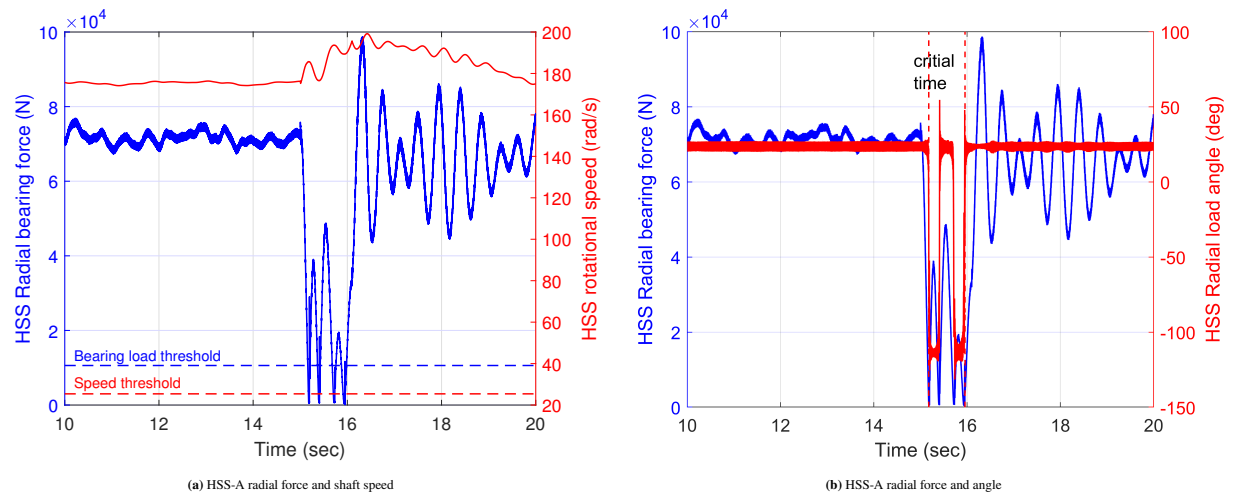
FIGURE 12 Main-shaft bearings

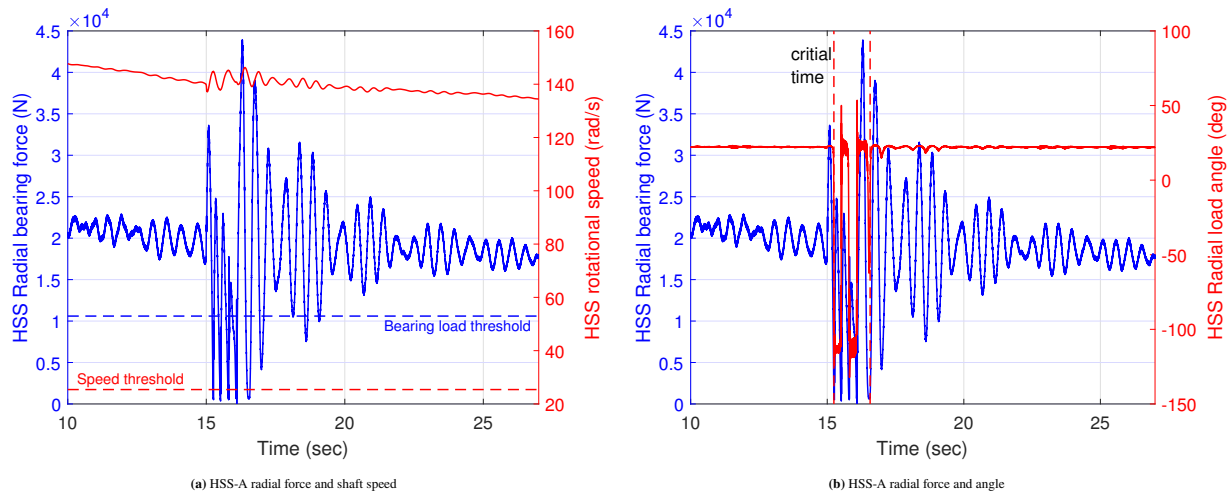**FIGURE 13** HSS-A radial bearing forces and high speed shaft speed at hub-height mean wind speed of 11m/s

(a) HSS-A radial force and shaft speed

(b) HSS-A radial force and angle

FIGURE 14 HSS-A radial bearing forces and high speed shaft speed at hub-height mean wind speed of 6m/s

(a) HSS-A radial force and shaft speed
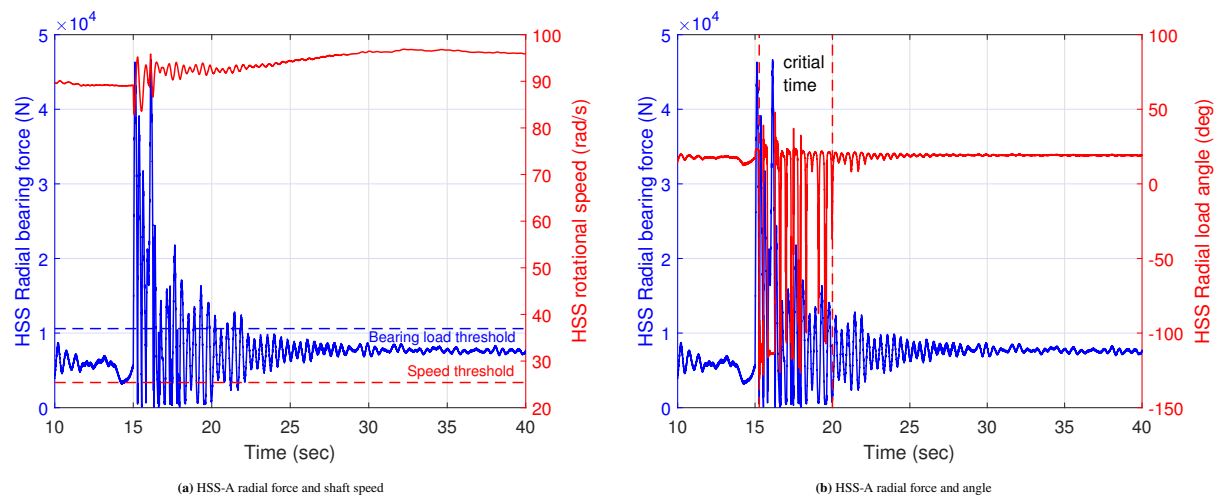
(b) HSS-A radial force and angle

FIGURE 15 HSS-A radial bearing forces and high speed shaft speed at hub-height mean wind speed of 4m/s

Although a multidimensional sensitivity analysis is required to study the sensitivity of four variables on the output, in a first attempt, the four variables are considered one at a time, keeping the other three fixed. The parameters of the sensitivity study are shown in Table 3, and the results are presented in Figure 17. The results show that the *slip risk duration* is sensitive to the wind speed and the turbulence intensity. However, it is less sensitive to the wind veer and rather insensitive to the vertical wind shear. Further investigation into the results presented in Figure 17 and the dynamics presented in Section 5.3 uncovers that the duration of the fault is typically less than one second, whereas the frequency content of the Kaimal spectrum used to generate the wind fields in TurbSim[32] results in a much larger time period for the dominating frequency content in the inflow wind as shown in Figure 16. Figure 16 shows that the wind speed during the duration of the fault is rather steady. Therefore, while the IEC guidelines generally recommend a 10 minute time history to derive wind inflow statistics, it can be inappropriate for instantaneous events that occur for a much shorter duration. Therefore, the sensitivity of the slip risk duration must be evaluated against the instantaneous wind speeds and is presented in the following section in Figure 17.
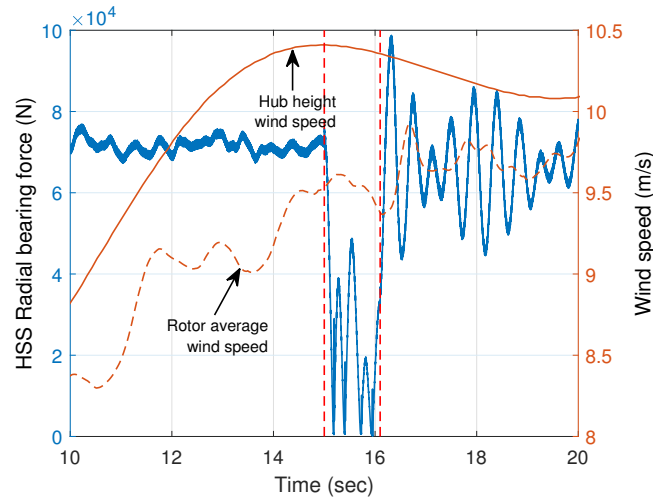
FIGURE 16 Wind speeds during grid fault

Figure #	Wind speed (m/s)	IEC Turbulence Class/Intensity	Vertical shear coefficient (α)	Wind veer angle (°)	No of seeds in each parameter set
Figure 17a	varies [4, 23]	NTM Class A	0.2	0	10
Figure 17b	12	varies [0.6, 0.26]	0.2	0	10
Figure 17c	12	NTM Class A	varies [0.1, 0.4]	0	10
Figure 17d	12	NTM Class A	0.2	varies [-10, 30]	10

TABLE 3 Parameters for inflow wind sensitivity analysis

5.5 | Case study of a Swedish wind farm

The Röbergsfjället wind farm, situated in mid-west Sweden, comprises of 8 Vestas V90-2.0[28] wind turbines that have a nominal electrical capacity of 2 MW. The generic 2MW wind turbine model developed to mimics the behaviours of these Vestas V90 is verified in Figure 18. The results in Figure 18 compare the electrical power output and the rotor speed measured by the SCADA system against the prediction obtained from the developed model. The SCADA data is scattered due to the stochastic nature of the measurement. However, the OpenFAST model prediction matches well with the measurements.

In a previous paper studying this wind farm[35], it was demonstrated that in complex terrain, the inflow wind properties varies at the different turbines situated in the same wind farm, demonstrating the importance of CFD tools to predict the wind flow in complex terrain. Along the same line of thinking, it is worth investigating how the underlying Kaimal spectrum used in TurbSim[32] compares against a site-specific flow field prediction obtained from CFD tools. To this end, the *slip risk duration* is plotted against the hub-height wind speeds, and the rotor averaged wind speed and the rotor torque, respectively, in Figure 19 at the time of the fault. The results show that while there is a significant dependence of the *slip risk duration* on the instantaneous wind speed/rotor torque at the time of the fault, the results predicted from the wind fields generated by TurbSim[32] match very well with site-specific wind fields from CFD analysis. The match is attributed to the separation of the dominant frequency content in the wind spectrum from the bearing response spectrum. The dominating trend to note is that the *slip risk duration* increases with decreasing wind speed because at lower wind speeds, the available torque required to stabilise the radial bearing load angle is lower. The results show that there is an increased risk of surface damage (like smearing and scuffing) at lower wind speeds due to grid faults compared to higher wind speeds. The case study of the wind farm naturally leads to the estimation of the number of transient events pertaining to DLC 2.1, 2.3 or 5.1 experienced by the eight turbines situated in the wind farm. The available 1.5 years (June 2017 to January 2019) SCADA data is scanned systematically to identify these events. First, cases
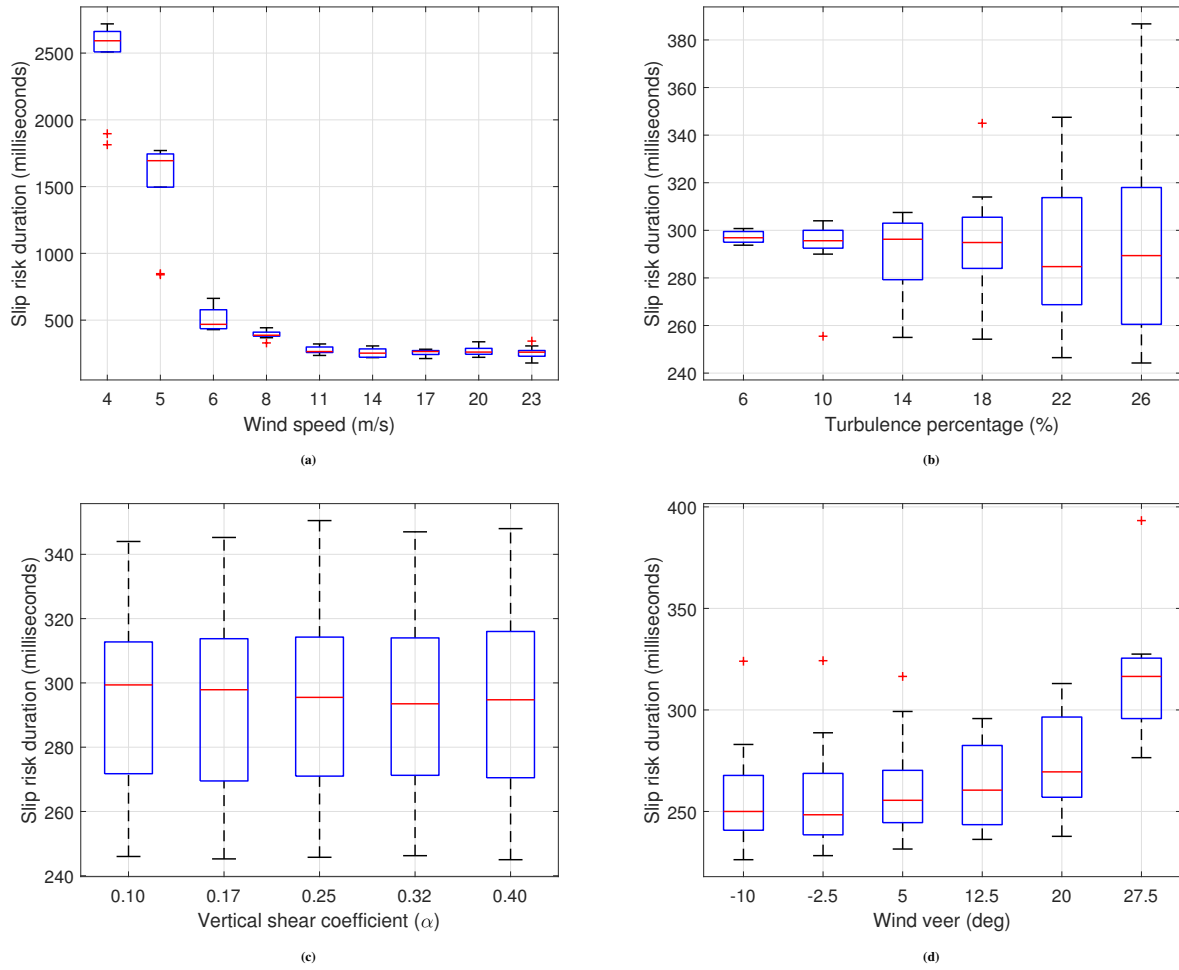
FIGURE 17 Statistics of slip risk duration w.r.t varying wind parameters
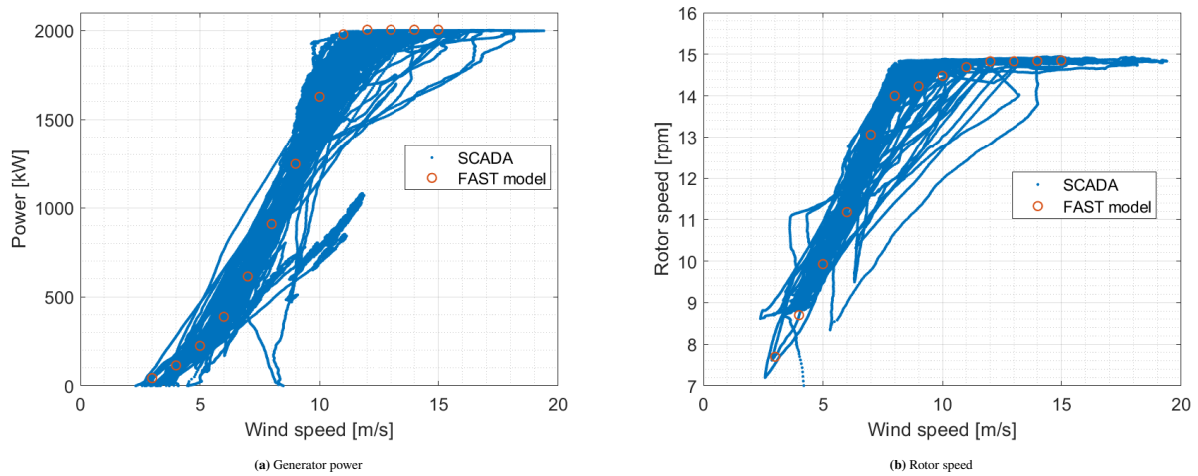

FIGURE 18 Comparison of SCADA data against OpenFAST model

pertaining to DLC 5.1 are identified. One instance of an emergency shutdown during a storm is presented in Figure 20. Figure 20 shows the SCADA measurements during the time of the shutdown for turbine number 6. The shutdown is initiated at 2019-01-01 20:19:56 due to high wind speed during the storm. A similar emergency shutdown was simulated using the developed numerical model and overlaid on the SCADA measurements. It can be observed that the system dynamics match well, further supporting the developed numerical model. The numerical model predicted the occurrence of TTRs during such events as events in Section 5.2 leading to the conclusion that these events will also induce TTRs in the field turbines that can lead to bearing damage. Scanning the data of all eight turbines showed that turbines 2, 6 and 7 experienced the least number (two) of emergency shutdowns and turbine 5 experienced the highest number (seventeen) of emergency shutdowns in the available 1.5 years of data. This emphasises that the number of transient events and the damage accumulated by the gearboxes varies significantly between turbines. Identifying DLCs 2.1 and 2.3 in the SCADA data is more challenging since the turbines are required to continue operation during these faults (fault ride-through capability). However, systematic scanning for the available SCADA data results in an estimate of 20-60 transient events per turbine pertaining to DLCs 2.1 and 2.3 in the available 1.5 years of SCADA data. As mentioned before, there is a high degree of variability in the number of transient events between turbines.

The results show that the wind turbines are frequently subjected to transient conditions that can lead to transient torque reversals. The perceived risk is lower at higher wind speeds due to the availability of aerodynamic torque required to return to stable operation.
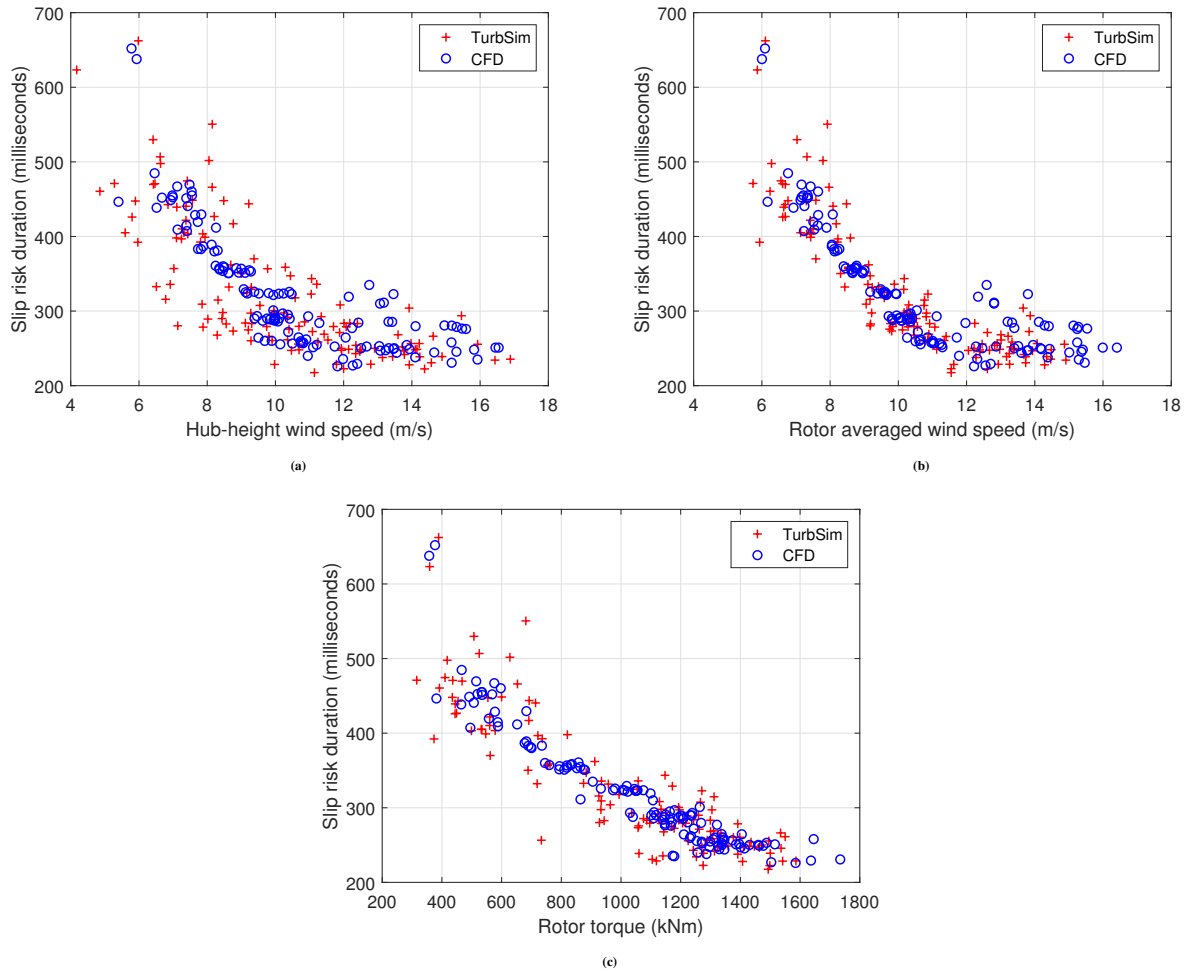

(a)

(b)

(c)

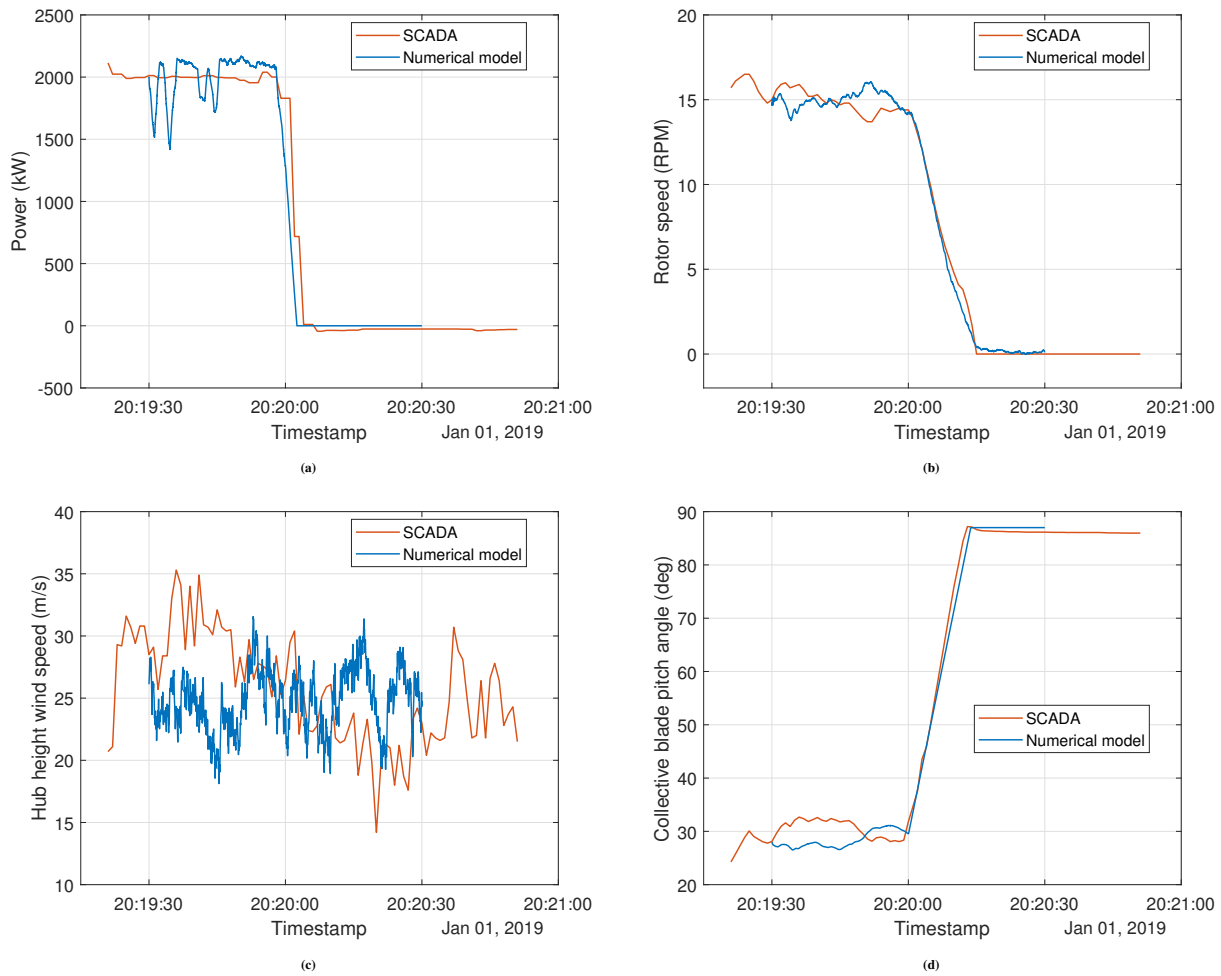**FIGURE 19** Sensitivity of slip risk duration to wind speeds and torque

FIGURE 20 Emergency shutdown – SCADA measurements vs numerical model prediction

6 | CONCLUSIONS

This paper presents an extensive investigation into Transient Torque Reversals (TTRs) using a numerical model of a 2 MW wind turbine and its dependence on inflow wind parameters. A range of IEC design load cases is investigated to identify the load cases that may lead to TTRs. Since TTRs have the most significant impact on drivetrain bearings, this paper focuses on the risk of damage associated with the bearings. It is hypothesised that the occurrence of TTRs (rapid reversal of bearing loading zone) coupled with high inner-raceway speeds increases the risk of surface damage on bearings rollers. With this in mind, the design load cases that simulate transient events, electrical faults and emergency shutdowns are of particular interest. These cases are important because: a) they induce TTRs while the rotational speed of the shaft/the inner-raceway speed of the bearings is high, and b) they are expected to occur with moderate frequency within the life of the turbine. The paper further investigates the dependence of TTRs on inflow wind parameters. A quantity termed as *slip risk duration* is proposed here to quantify the induced risk of damage. The two most important conclusions drawn from the investigation are: a) due to the faster dynamics and shorter duration of the events, the correlation between the risk of induced damage and the wind is better represented by the instantaneous wind speed at the time of the fault rather than the 10 minutes statistics which is typically used to quantify wind parameters, and b) the risk of induced damage is higher at lower wind speeds due to the reduced availability of aerodynamic torque required to stabilise the bearing forces.

The results presented in this paper and the literature point out that transients in the generator electromagnetic torque impose a degree of damage risk on the wind turbine bearings. With the increased wind energy penetration in the electricity grid, wind energy is now required to provide essential reliability services or ancillary services. Naturally, wind turbines will be expected to

ride through various electrical events such as voltage drops and frequency variations and provide ancillary services in the form of reactive current and frequency response. The correlation between the severity of the TTRs and the inflow wind presented in this paper indicates that the turbines operating at or near their rated capacity are better suited to ride through electrical faults (grid faults) than the turbines operating well below their rated capacity. Future work is underway to determine the suitability of turbines to provide ancillary services based on their operating point.

ACKNOWLEDGMENTS

☐

APPENDIX

A DESIGN DATA OF A GENERIC 2 MW WIND TURBINE, DRIVETRAIN AND GENERATOR

Class	IEC IIA
Rotor	
Diameter	90 m
Swept area	6362 m^2
Rated rotational speed	14.75 RPM
Rotational speed range	9.6-17.0 RPM
Cut-in, cut-out wind speeds	3.5 m/s, 25 m/s
Rotational direction	Clockwise (from front)
Type	Upwind
Tilt	6°
Cone	2°
Number of blades	3
Aerodynamic brakes	Full feathering
Blades	
Length	44 m
Maximum cord length	3.512 m
Blade tip cord	0.391 m
Twist at the root	27°
Approximate weight	6750 kg
Gearbox	
Type	1 planetary stage + 2 helical stages
Ratio	113.88
Tower	
Type	Conical tubular
Hub height	80 m
Weight	125 metric tonnes
Generator 2.0 MW	
Type	Asynchronous, wound rotor, slip rings and VCS
Rated power	2.0 MW
Frequency	50 Hz
Voltage, Generator	690 Vac
Number of poles	4
Approximate weight	7500 kg
Converter 2.0 MW	
Rated slip	12%
Rated RPM	1680 RPM
Rated rotor power (@ rated slip)	214 kW

TABLE A1 Generic 2MW wind turbine specifications

Gear	Type	Normal module (mm)	Normal pressure angle (°)	Helix angle (°)	No of teeth (mm)	Flank width (mm)
Planet	Internal	16	20	6	35	320
Sun	Internal	16	20	6	19	320
Ring	External	16	20	6	89	320
Gear 1	Internal	12	20	10	85	215
Pinion 1	Internal	12	20	10	19	215
Gear 2	Internal	6.5	20	16.5	103	150
Pinion 2	Internal	6.5	20	16.5	23	150

TABLE A2 Gear data

Name	Type	Model	No of rows	Roller diameter (mm)	Effective roller length (mm)	No of rollers	Pitch radius (mm)	Contact angle (°)
INP A	Spherical	241/600 ECAK30/W33	2	101.4	148.4	21	398.4	13
INP B	Spherical	241/530 ECAK30/W33	2	90.0	132.8	21	352.8	13
PLC A	Cylindrical	NCF 18/560 V/HB1	1	32.0	30.0	61	311.5	–
PLC B	Cylindrical	NCF 2984 V	1	38.0	62.0	40	243.0	–
PLx A/B	Cylindrical	NU 2344 ECMA	2	68.0	101.7	14	172.5	–
LSS A	Spherical	23984 CC/W33	2	32.5	37.8	40	247.4	6
LSS B	Spherical	23992 CAK/W33	2	37.5	43.0	38	272.6	6
IMS A	Cylindrical	NU 2338 ECML	1	60.0	95.5	13	150.0	–
IMS B	Cylindrical	NU 2340 ECML	1	62.0	100.0	13	157.5	–
IMS C	Ball	QJ 338 N2MA	1	63.5	–	12	147.5	35
HSS A	Cylindrical	NU 2234 ECML	1	38.0	62.0	16	121.5	–
HSS B	Cylindrical	NU 232 ECM	1	32.0	32.0	19	113.5	–
HSS C	Ball	QJ 328 N2MA	1	47.6	–	12	110.0	35

TABLE A3 Bearing data

Parameter	Value	Remark
Synchronous speed	1500 rpm	Synchronous speed at 50 Hz
Rated power	2 MW	Nominal stator three-phase active power
Rated stator voltage	690 V$_{rms}$	Line-to-line nominal stator voltage
Rated stator current	1760 A$_{rms}$	Each phase nominal stator current
Rated torque	12.7 kNm	Nominal torque
p	2	Number of pole pairs
u	1/3	Stator/Rotor turn ratio
R_s	2.6 mΩ	Stator resistance
$L_{\sigma s}$	87 μH	Stator leakage inductance
L_m	2.5 mH	Magnetizing inductance
R'_r	26.1 mΩ	Rotor resistance
$L'_{\sigma r}$	783 μH	Rotor leakage inductance
R_r	2.9 mΩ	Rotor resistance referred to the stator
$L_{\sigma r}$	87 μH	Rotor leakage inductance referred to the stator
L_s	2.587 mH	Stator inductance, $L_s = L_m + L_{\sigma s}$
L_r	2.587 mH	Rotor inductance, $L_r = L_m + L_{\sigma r}$

TABLE A4 Electrical parameters of the double fed induction generator model[36]

References

1. Council GWE. GWEC| global wind report 2021. *Global Wind Energy Council: Brussels, Belgium* 2021.

2. Sheng S. Report on wind turbine subsystem reliability-a survey of various databases (presentation). tech. rep., National Renewable Energy Lab.(NREL); Golden, CO (United States): 2013.

3. Musial W, Butterfield S, McNiff B. Improving wind turbine gearbox reliability. tech. rep., National Renewable Energy Lab.(NREL); Golden, CO (United States): 2007.

4. Evans RD, Barr TA, Houpert L, Boyd SV. Prevention of smearing damage in cylindrical roller bearings. *Tribology Transactions* 2013; 56(5): 703–716.

5. Evans MH. An updated review: white etching cracks (WECs) and axial cracks in wind turbine gearbox bearings. *Materials Science and Technology* 2016; 32(11): 1133–1169.

6. Stadler K, Lai J, Vegter R. A review: the dilemma with premature white etching crack (WEC) bearing failures. *Bearing Steel Technologies: 10th Volume, Advances in Steel Technologies for Rolling Bearings* 2015.

7. Sharpley N. Understanding the root causes of axial cracking in wind turbine gearbox bearings. https://www.windpowerengineering.com/understanding-root-causes-axial-cracking-wind-turbine-gearbox-bearings/; 2014.

8. Scherb B, Zech J. *A Study on the Smearing and Slip Behaviour of Radial Cylindrical Roller Bearings*. Georg-Simon-Ohm-Fachhochschule, NürnbergGeorg-Simon-Ohm-Fachhochschule . 2001.

9. Hamer JC, Sayles RS, Ioannides E. An Experimental Investigation Into the Boundaries of Smearing Failure in Roller Bearings. *Journal of Tribology* 1991; 113(1): 102-109. doi: 10.1115/1.2920573

10. Fowell M, Ioannides S, Kadiric A. An experimental investigation into the onset of smearing damage in nonconformal contacts with application to roller bearings. *Tribology Transactions* 2014; 57(3): 472–488.

11. Selvaraj A, Marappan R. Experimental analysis of factors influencing the cage slip in cylindrical roller bearing. *The International Journal of Advanced Manufacturing Technology* 2011; 53(5-8): 635–644.

12. Ruellan A, Cavoret J, Ville F, Kleber X, Liatard B. Understanding white etching cracks in rolling element bearings: state of art and multiple driver transposition on a twin-disc machine. *Proceedings of the Institution of Mechanical Engineers, Part J: Journal of Engineering Tribology* 2017; 231(2): 203–220.

13. Torrance A, Cameron A. Surface transformations in scuffing. *Wear* 1974; 28(3): 299–311.

14. Harada H, Mikami T, Shibata M, Sokai D, Yamamoto A, Tsubakino H. Microstructural changes and crack initiation with white etching area formation under rolling/sliding contact in bearing steel. *ISIJ international* 2005; 45(12): 1897–1902.

15. Bujoreanu C, Cretu S, Nelias D. Scuffing behaviour in angular contact ball-bearings. *The Annals of "Dunarea de Jos" University of Galati, Fascicle VIII, Tribology* 2003: 33–39.

16. Kelley B. A new look at the scoring phenomena of gears. *SAE transactions* 1953: 175–188.

17. Bowman W, Stachowiak G. A review of scuffing models. *Tribology Letters* 1996; 2(2): 113–131.

18. Dyson A. The failure of elastohydrodynamic lubrication of circumferentially ground discs. *Proceedings of the Institution of Mechanical Engineers* 1976; 190(1): 699–711.

19. Cheng H, Dyson A. Elastohydrodynamic lubrication of circumferentially-ground rough disks. *Asle Transactions* 1978; 21(1): 25–40.

20. Eatherton S, Moroz E, Sadler D, Heidenreich D. FMEA shows transient torsional events damage more than gearbox bearings. https://www.windpowerengineering.com/fmea-shows-transient-torque-events-damage-gearbox-bearings/; 2016.

21. Blockmans B, Helsen J, Vanhollebeke F, Desmet W. Dynamic response of a multi-megawatt wind turbine drivetrain under voltage dips using a coupled flexible multibody approach. In: . 55928. American Society of Mechanical Engineers. ; 2013: V005T11A045.

22. Röder J, Jacobs G, Duda T, Bosse D, Herzog F. Simulative investigation of wind turbine gearbox loads during power converter fault. *Forschung im Ingenieurwesen* 2021; 85(2): 251–256.

23. Röder J, Jacobs G, Duda T, Bosse D, Herzog F. Investigation of Dynamic Loads in Wind Turbine Drive Trains Due to Grid and Power Converter Faults. *Energies* 2021; 14(24): 8542.

24. SIMPACK 2020x.2. https://www.3ds.com/products-services/simulia/products/simpack/; 2020. Accessed: 2021-11-11.

25. Jonkman J, Buhl Jr M. FAST user's guide.. *National Renewable Energy Laboratory, Golden, CO, Technical Report No. NREL/EL-500-38230* 2005.

26. Commission IE, others . Wind turbines-part 1: design requirements. *IEC 614001 Ed. 3* 2006.

27. Jonkman J, Butterfield S, Musial W, Scott G. Definition of a 5-MW reference wind turbine for offshore system development. tech. rep., National Renewable Energy Lab.(NREL); Golden, CO (United States): 2009.

28. Vestas Wind Systems A/S . General Specification V90–1.8/2.0 MW 50 Hz VCS. http://ventderaison.eu/gembloux/eie_ABO-WIND/Annexes/Annexe_N_1_Courbe_acoustique_V90.pdf; 2010. Online; accessed 23-April-2021.

29. Abu-Rub H, Malinowski M, Al-Haddad K. *Power electronics for renewable energy systems, transportation and industrial applications*. John Wiley & Sons . 2014.

30. NREL . OpenFAST v3.0.0. https://github.com/OpenFAST/openfast/releases/tag/v3.0.0/; 2021. Online; accessed 03-February-2022.

31. Girsang IP, Dhupia JS, Muljadi E, Singh M, Pao LY. Gearbox and drivetrain models to study dynamic effects of modern wind turbines. *IEEE Transactions on Industry Applications* 2014; 50(6): 3777–3786.

32. Jonkman BJ. TurbSim user's guide: Version 1.50. tech. rep., National Renewable Energy Lab.(NREL); Golden, CO (United States): 2009.

33. Jiang Z, Xing Y. Load mitigation method for wind turbines during emergency shutdowns. *Renewable Energy* 2021.

34. Robertson AN, Shaler K, Sethuraman L, Jonkman J. Sensitivity analysis of the effect of wind characteristics and turbine properties on wind turbine loads. *Wind Energy Science* 2019; 4(3): 479–513.

35. Abedi H, Sarkar S, Johansson H. Numerical modelling of neutral atmospheric boundary layer flow through heterogeneous forest canopies in complex terrain (a case study of a Swedish wind farm). *Renewable Energy* 2021; 180: 806–828.

36. Abad G, Lopez J, Rodriguez M, Marroyo L, Iwanski G. *Doubly fed induction machine: modeling and control for wind energy generation*. John Wiley & Sons . 2011.